THE UNIVERSITY *of* EDINBURGH



# A multilayer thermo-elastic damage model for the bending deflection of the tunnel lining segment exposed to high temperatures

**Citation for published version:**
Yan, Z, Zhang, Y, Shen, Y, Zhu, H & Lu, Y 2020, 'A multilayer thermo-elastic damage model for the bending deflection of the tunnel lining segment exposed to high temperatures', *Tunnelling and Underground Space Technology*, vol. 95, 103142, pp. 1. https://doi.org/10.1016/j.tust.2019.103142

**Digital Object Identifier (DOI):**
10.1016/j.tust.2019.103142



**Document Version:**
Peer reviewed version

**Published In:**
Tunnelling and Underground Space Technology

# A multilayer thermo-elastic damage model for the bending deflection of the tunnel lining segment exposed to high temperatures

Zhi-guo Yan [a,b,c], Yao Zhang [b,c], Yi Shen [a,b,c], He-hua Zhu [a,b,c], Yong Lu [d]

[a] State Key Laboratory of Disaster Reduction in Civil Engineering, Tongji University, 1239 Siping Road, Shanghai 200092, China

[b] Department of Geotechnical Engineering, Tongji University, 1239 Siping Road, Shanghai 200092, China

[c] Key Laboratory of Geotechnical and Underground Engineering of the Ministry of Education, Tongji University, 1239 Siping Road, Shanghai 200092, China

[d] Institute for Infrastructure and Environment, School of Engineering, University of Edinburgh, Edinburgh EH9 3JL, UK

**Abstract:** For a shield tunnel structure in fire, the thermal-mechanical behavior of tunnel lining segments plays a key role in determining the failure process. Due to the restriction at the segment ends, secondary stress will be induced, and this is particularly the case when the temperature distribution is non-uniform over the cross-section, thus further worsening the adverse effect on the structure. Existing studies on the thermal-mechanical behavior of tunnel lining have mainly focued on the complex nonlinear and non-elastic behavior of the concrete, whereas little attention has been paid to the application in engineering. In this study, a multilayer thermo-elastic damage model is proposed to analyze the bending behavior of the tunnel lining segment exposed to high temperature. The temperature distribution on the cross-section is described by a piecewise function. The contributions of the concrete and bolts are modelled equivalently by a set of springs. A multi-scale thermal damage model is introduced to describe the damage evolution of concrete with temperature. Various boundary conditions, including a statically determinate segment, a statically indeterminate segment with two hinged ends and a segment with two fixed ends, are considered. To verify the analytical model, four-point bending tests have been conducted with reduced-scale specimens. Test results indicate that this multilayer model can well predict the response of the tunnel lining segment under or after high temperature. The model is suitable in the fire protection design of the tunnel lining segment.

**Keywords:** tunnel segment; fire; multi-layer model; fire pretection design.

# 1. Introduction

There have been numerous serious tunnel fires worldwide, causing significant number of casualties and considerable property damages. For example, in the Tauern Tunnel fire in 1999, 12 people were killed, and 60 people were injured (Gandit et al., 2009); in the Mont Blanc Tunnel fire (France-Italy) in 1999, 39 people were killed (Vuilleumier et al.,2002). These catastrophic tunnel fire incidents certainly highlighted the importance of fire safety in tunnel design, and they also raised further attention to reliable and effective tunnel structures (Beard, 2009). For a tunnel, because of its confined space and insufficient exits, fires usually result in fast temperature rise and high peak temperature (Nilsson et al., 2009), posing serious threat to the tunnel lining structure itself.

Under elevated temperature, the damage to the tunnel lining segment can be caused by degradation of the mechanical property of concrete, as well as area reduction in the cross-section of lining segment (Chen and Liu, 2004; Yan et al., 2012; Yan et al., 2013; Shen et al., 2015; Yan et al., 2015; Yan et al., 2016). High temperature beneath the tunnel ceiling above 250℃ could induce surface layer of concrete falling out from the tunnel structure, and progressive spalling can follow. Spalling is in fact a very complex phenomenon, which has attracted a lot of research interest. However, there exist some different views about the mechanisms of concrete explosive spalling (Kodur, 2014). Some works (Kalifa et al., 2000; Phan et al., 2001) tend to show that the spalling of concrete is caused by pore pressure built-up. This adverse effect can be alleviated through the addition of polypropylene fibers since such fibres can create microchannels after melting (Kalifa et al., 2001; Bangi and Horiguchi, 2012; Mindeguia et al., 2010; Li and Liu, 2016). On the other hand, restrained thermal dilatation is also considered as a factor influencing the spalling (Ulm et al., 1999 a&b; Haddad and Shannis, 2004).

To analyse the mechanisms of concrete spalling under high temperature, formulations of partial differential equations based on the laws of thermodynamics from the material level, taking into account of porosity, humidity, mass and heat transfer have been put forward (Schrefler et al., 2014; Gawin et al., 2003; Gawin et al., 2006; Gawin et al., 2010), while the finite difference method and the finite element method are generally employed to obtain the solution. To reflect the thermo-mechanical behavior of concrete, constitutive relations based on internal variable theory have been proposed (Ulm et al., 1999 a&b; Ju et al., 1998).

The structural behavior of the tunnel lining segments in fire have been investigated using four-point bending tests at elevated temperature (Yan et al., 2012; Yan et al., 2013). On the other hand, semi-analytical or numerical methods have been employed to analyse the mechanical performance of the tunnel lining segment at elevated temperature (Choi et al., 2013).

In general, the models for the analysis of tunnel segmental lining can be classified as the continuous model and the discontinuous model. The continuous model assumes that tunnel lining is an entire ring with uniform flexural rigidity. A reduction factor is introduced to correct the effect of joints on the bending stiffness of the tunnel lining. In the discontinuous model, the segments and joints are simplified as a group of springs with equivalent bending stiffness, axial stiffness and shear stiffness (Li et al., 2015; Blom, 2002). Past experiments have shown that the stiffness at a joint exhibits a bilinear behavior when the joint gradually loses contact, and this behavior can be well characterized by a progressive model (Li et al., 2015; Koyama, 2002; Klappers et al., 2006; Zhu, 1995). Other models have been formulated to analyze the mechanical behavior of the tunnel lining segments in three-dimensional space (Molins and Arnau, 2011; Liu, 2014; Huang, 2006; Zhu et al., 2006).

Under high temperature, because of the presence of steel bars at specific locations in the radial direction, the coefficient of heat conduction of a reinforced concrete component is not uniform. Thus, using a multilayer model is a ratioanl and effective approach. Guo and Shi

(2003) developed a combined model to analyze the mechanical behavior of concrete components in fire. The interface between the steel bar and concrete was assumed to be perfect and non-slipping. The reinforced concrete section was divided into many stripes with the assumption that the stress on each stripe was uniformly distributed. Results illustrated that the satisfactory relationship between bending moment and curvature could be achieved by using 7-10 stripes (Ibañez et al., 2013; Li. 2007; Kodur and Sultan, 2003; Kudor and Yu, 2013; Kudor et al., 2005). Another method, named fiber model, has also been used, in which the cross-section is divided into different regions based on the mechanical properties of the material in the specimen (Chen et al., 2009; Chen and Ren, 2011). The arrangement and material properties of the reinforcement are taken into consideration in this model, and the the influence of combined bending moment and axial force can be represented.

Using the multi-layer composite material approach, Wang and Meng (1998) and Han et al. (2010) presented the analytical solution of displacement of laminated composite beams under special loads. Chen and Ren (2011) used a novel numerical model based on the fiber beam model and multi-layer shell element to analyze and simulate the collapse of reinforced concrete frame structure under fire, . Yin and Wang (2004; 2005 a&b) presented a method to describe the irregular temperature distribution in steel beams under elevated temperature.

It should be noted that most of the experimental and analytical investigations into the thermo-mechanical behaviors of of reinforced concrete under high temperatures have been conducted on straight beams or plates. Reseach on the modeling of the thermo-mechanical behaviors of the curved beams, in connection with tunnel design in fire, is scarce. Among the existing studies, Li and Zhou (2008) adopted the geometric nonlinearity theory of Euler-Bernoulli beam and formulated governing equations for the elastic curved beam under the combination of thermal and mechanical load. Heidarpour et al. (2009; 2010 a&b&c) conducted a series of studies about the steel-concrete curved beams under fire, and proposed analysis method which was validated by finite element method (FEM). A thermo-hydro-mechanical (THM) coupling model was adopted by Ružić et al. (2015) to analyze the response of the reinforced concrete curved beam under high temperature. These existing models can reasonably describe the mechanical behaviors of the curved beam under fire. However, due to the complexity in the formulations, the solution requires complicated numerical procedures, making these models difficult to apply in the tunnel structural design.

In this paper, we focus on developing an analytical model, with progressive thermal damage, for the bending behavior of the tunnel lining segment based on the combination of curved beam theory. A thermo-mechanical model is derived for the reinforced concrete tunnel lining segment in a given fire condition. To verify the soundness of the model, four-point bending tests are conducted with reduced-scale specimens. Comparison with the test results indicates that the proposed multilayer model can well predict the response of the tunnel lining segment under or after elevated temperatures. The method is simple to implement and therefore is suitable for the fire protection design of the tunnel lining segment.

# 2. Theoretical development

## 2.1 Sectional analysis

The following assumptions have been adopted to facilitate the multilayer model development of tunnel lining segment subjected to a fire.

1) Concrete is isotropic at the macro level and the damage caused by temperature is also isotropic at each layer.

2) The bolts and the corresponding bolt holes are in close contact, and so no additional deformation is induced at such contacts.

3) Small deformation is assumed. Thus, the bending deformation of the tunnel lining segment has a negligible impact on the internal force distribution.

A tunnel lining segment cross-section subjected to bending moment and the axial thrust is divided into multiple layers according to the distribution of mechanical and thermal properties on the section. The plane cross-section assumption is adopted to derive the stress on the cross-section. Thus the strain on this section can be expressed as:

$$\varepsilon_t = (y + y_n)\kappa \tag{1}$$

where $\kappa$ is the curvature and $y_n$ is the height of the compressive zone and it ranges from 0 to $h$.

At a fixed time point, the thermal distribution $T_\alpha(y)$ on the section of the tunnel lining segment is assumed to be known. As shown in **Fig.1**, $T_\alpha(y)$ may be expressed by a piecewise linear function as follows:

$$T_\alpha(y) = T_t + y\nabla_\alpha + \widetilde{\nabla}_\alpha \qquad (\alpha = 1, 2, \cdots, n) \tag{2}$$

$$\nabla_\alpha = \frac{T_\alpha - T_{\alpha+1}}{h_\alpha}, \ \widetilde{\nabla}_\alpha = \sum_1^\alpha h_{\alpha-1}\nabla_{\alpha-1} \tag{3}$$

where $h_\alpha$ is the height of the arbitrary layer; at $h_0$=0, $\nabla_0$=0, $\alpha$=1. $n$ is the total number of layers for the cross-section. Generally, the elastic strain $\varepsilon_e$ can be defined as equal to the total strain $\varepsilon_t$ minus the thermal strain $\varepsilon_\theta$:

$$\varepsilon_e = \varepsilon_t - \varepsilon_\theta \tag{4}$$

where the thermal strain can be written as: $\varepsilon_\theta\left(y\right) = \lambda_\alpha T_\alpha(y)$, where $\lambda_\alpha$ is the coefficient of linear expansion; $T_\alpha(y)$ is the thermal distribution function of layer $\alpha$.

Thus the normal stress on the section can be obtained:

$$\sigma_\alpha = E_T(y)\varepsilon_e = E_T(y)\bullet(-\varepsilon_c + y_n\kappa + y(\kappa - \lambda_\alpha\nabla_\alpha)) \tag{5}$$

where $E_T(y)$ corresponds to Young's modulus at $y$ where the temperature is $T$. $\varepsilon_c$ in Eq.(5) can be given by:

$$\varepsilon_c = \lambda_\alpha (T_t + \widetilde{\nabla}_\alpha) \tag{6}$$

Further, the axial thrust can be obtained through the integration:

$$N_\alpha = \int_{A_\alpha} \sigma_\alpha dA_\alpha = -(\varepsilon_c - y_n \kappa)\overline{EA_\alpha} + (\kappa - \lambda_\alpha \nabla_\alpha)\overline{EB_\alpha} \quad (\alpha = 1, 2, \cdots, n) \tag{7}$$

where $\overline{(EA)}_\alpha = \int_{A_\alpha} E_T^\alpha(y) dA_\alpha$, $\overline{(EB)}_\alpha = \int_{A_\alpha} y E_T^\alpha(y) dA_\alpha$. It should be noted that when layer $\alpha$ contains steel bars, $E_T^\alpha(y)$ can be determined through the mechanics of composite materials, as follows:

$$E_T^\alpha(y) = \frac{E_c A_c + E_s A_s}{A_c + A_s} \tag{8}$$

where $E_c$ and $E_s$ are the Young's modulus of concrete and steel bar, respectively; $A_c$ and $A_s$ are the section area of the concrete and steel bar in the layer, respectively.

The height of compressive region can be obtained as:

$$y_n = \frac{1}{\sum_{\alpha=1}^{n} \overline{(EA)}_\alpha} \left( \sum_{\alpha=1}^{n} \overline{(EB)}_\alpha - \frac{N_{\text{int}} + N_\Pi}{\kappa} \right) \tag{9}$$

where $N_{\text{int}} = \sum_{\alpha=1}^{n} N_\alpha$, and $N_\Pi = \sum_{\alpha=1}^{n} (\lambda_\alpha \nabla_\alpha \overline{(EB)}_\alpha + \varepsilon_c \overline{(EA)}_\alpha)$.

In a similar way, the bending moment at layer $\alpha$ can be obtained by:

$$M_\alpha = \int_A \sigma_\alpha y dA_\alpha = -(\varepsilon_c - y_n \kappa)\overline{(EB)}_\alpha + (\kappa - \lambda_\alpha \nabla_\alpha)\overline{(EI)}_\alpha \tag{10}$$

where the flexural stiffness $\overline{(EI)}_\alpha = \int_{A_\alpha} y^2 E_T^\alpha(y) dA_\alpha$.

Therefore, the expression of the compressive height can be re-written as:

$$y_c = \frac{1}{\sum_{\alpha=1}^{n} \overline{(EB)}_\alpha} \left( \sum_{\alpha=1}^{n} \overline{(EI)}_\alpha - \frac{M_{\text{int}} + M_\Pi}{\kappa} \right) \tag{11}$$

where $M_{\text{int}} = \sum_{\alpha=1}^{n} M_\alpha$, $M_\Pi = \sum_{\alpha=1}^{n} (\lambda_\alpha \nabla_\alpha \overline{(EI)}_\alpha + \varepsilon_c \overline{(EB)}_\alpha)$.

According to the compatibility of Eqs. (9) and (11), the curvature can be obtained as:

$$\kappa = \frac{\sum_{\alpha=1}^{n}\overline{(EA)_\alpha}}{\left(\sum_{\alpha=1}^{n}\overline{(EA)_\alpha}\right)\left(\sum_{\alpha=1}^{n}\overline{(EI)_\alpha}\right)-\left(\sum_{\alpha=1}^{n}\overline{(EB)_\alpha}\right)^2}\left[M_{\text{int}}+M_{\Pi}-\frac{\sum_{\alpha=1}^{n}\overline{(EB)_\alpha}}{\sum_{\alpha=1}^{n}\overline{(EA)_\alpha}}\left(N_{\text{int}}+N_{\Pi}\right)\right] \tag{12}$$

## 2.2 Analysis of tunnel lining segment under general boundary conditions

In reality, the pressure from the soil and water loaded on the lining segment is continuous. In analysis, the continuously distributed pressure is usually represented by equivalent point loadings to analyze the bending behavior of the tunnel lining segment (Shen et al., 2015; Yan et al., 2016; Yan, 2007). Similar simplification is also adopted in the experiments (Shen et al., 2015; Yan et al., 2016).

The multilayer model described in Section 2.1 is verififed by comparing with the experimental data in this section. As in the test, a symmetrical arrangement of point loads is adopted, as shown in **Fig. 2**. To simulate the boundary conditions induced by the bolts and the connected lining segments, a set of horizontal, vertical and rational springs with equivalent stiffness are adopted at the segment ends. $k_{0h}$ , $k_{0v}$ and $k_{0r}$ are horizontal, vertical and bending stiffness at the left end, respectively, and $k_{Lh}$ , $k_{Lv}$ and $k_{Lr}$ are the corresponding stiffness at the other end (See **Fig.2**). The stiffnesses at the two ends are not the same in general conditions.

The internal force of the tunnel lining segment can be solved through the force equilibrium condition. The bending moment at any section along the segment length can be obtained as:

$$M_{\text{int}} = M_0 - H_0 y^* + V_0 z^*, z^* \le \frac{L}{2} - l \tag{13}$$

$$M_{\text{int}} = M_0 - H_0 y^* + V_0 z^* - F\left(z^* + l - \frac{L}{2}\right), \frac{L}{2} - l < z^* \le \frac{L}{2} + l \tag{14}$$

$$M_{\text{int}} = M_0 - H_0 y^* + V_0 z^* - 2Fl, z^* > \frac{L}{2} + l \tag{15}$$

where $y^* = R\left[\cos\varphi - \cos\left(\frac{\Theta}{2}\right)\right]$, $z^* = R\left[\sin\left(\frac{\Theta}{2}\right) + \sin\varphi\right]$, $L$ is the span of the segment, $l$ is the distance between the axis line and the applied force. $H_0$、$V_0$、$M_0$ are the horizontal, vertical and bending moment reactions at the origin of the coordinates (See **Fig. 2**). It should be noted that $H_0$、 $V_0$ are positive when their directions are consistent with the positive direction of the respective coordinate axis, while $M_0$ is positive if it is in a counter-clockwise direction.

The axial thrust of the section can be obtained as:

$$N_{\text{int}} = H_0 \cos\varphi + V_0 \sin\varphi, z^* \leq \frac{L}{2} - l \tag{16}$$

$$N_{\text{int}} = H_0 \cos\varphi + V_0 \sin\varphi - F \sin\varphi, \frac{L}{2} - l < z^* \leq \frac{L}{2} + l \tag{17}$$

$$N_{\text{int}} = H_0 \cos\varphi + V_0 \sin\varphi - 2F \sin\varphi, z^* > \frac{L}{2} + l \tag{18}$$

Finally the shear forces of the section can be obtained as:

$$V_{\text{int}} = H_0 \sin\varphi - V_0 \cos\varphi, z^* \leq \frac{L}{2} - l \tag{19}$$

$$V_{\text{int}} = H_0 \sin\varphi - V_0 \cos\varphi + F \cos\varphi, \frac{L}{2} - l < z^* \leq \frac{L}{2} + l \tag{20}$$

$$V_{\text{int}} = H_0 \sin\varphi - V_0 \cos\varphi + 2F \cos\varphi, z^* > \frac{L}{2} + l \tag{21}$$

For the convenience of expression, it can be defined as follows.

$$\varphi = -\Phi, z^* = \frac{L}{2} - l, \varphi = \Phi, z^* = \frac{L}{2} + l \tag{22}$$

where $\Phi$ is the central angle of the curve between the loading point and the midpoint of lining segment.

### 2.3 Displacement derivation under general boundary conditions

#### 2.3.1 Radial (lateral) displacement

The relationship between curvature, bending angle and radial (lateral) displacement follows the Euler beam theory:

$$\kappa = \frac{d\theta}{ds} = \frac{d^2 v}{ds^2} \tag{23}$$

where $s$ is is the tangential coordinate of the arch-shaped lining segment profile. When it satisfies $z^* \le \frac{L}{2} - l$, the curvature can be obtained:

$$\kappa = \lambda \left[ M_0 + M_\Pi - H_0 \left( y^* + \frac{\sum_{\alpha=1}^{n} \overline{(EB)_\alpha}}{\sum_{\alpha=1}^{n} \overline{(EA)_\alpha}} \cos\varphi \right) + V_0 \left( z^* - \frac{\sum_{\alpha=1}^{n} \overline{(EB)_\alpha}}{\sum_{\alpha=1}^{n} \overline{(EA)_\alpha}} \sin\varphi \right) - \frac{\sum_{\alpha=1}^{n} \overline{(EB)_\alpha}}{\sum_{\alpha=1}^{n} \overline{(EA)_\alpha}} N_\Pi \right] \tag{24}$$

Then using Eq. (23), the bending angle $\theta$ and radial displacement can be derived by integrating the $\kappa - \theta$ and $\kappa - v$ relations, as shown in Eq. (B1) and (B2) in the Appendix. Similarly, when $z^*$ satisfies $\frac{L}{2} - l < z^* \le \frac{L}{2} + l$ and $z^* > \frac{L}{2} + l$, the corresponding bending angle $\theta$ and radial displacement $v$ can be obtained, as shown in Eqs. (B3)-(B6) in Appendix. Details of the determination of the associated intregation constants can be found in Appendix. The expression of the parameter $\lambda$ is listed in the Eq. (A1).

2.3.2 Tangential displacement $u$

According to Bradford (2006, 2011), the geometric relation between strain and tangential displacement $u$ of a curved beam section can be given by:

$$\varepsilon_t = \frac{du}{ds} + \frac{1}{2}\left(\frac{dv}{ds}\right)^2 - \frac{v}{R} - y\left(\frac{d^2 v}{ds^2}\right) \tag{25}$$

The tangential displacement can be derived if Eq. (25) equals Eq. (1) at $y=0$:

$$u(s) = \int \left[ -y_n \kappa - \frac{1}{2}\left(\frac{dv}{ds}\right)^2 + \frac{v}{R} \right] ds + C_{e3} \qquad e = 1,2,3 \tag{26}$$

For z$^*$ falling into three different intervals, the corresponding tangential displacement $u$ can be obtained, respectively, as can be seen in detail in Eqs. (C1)- (C10) in Appendix.

2.3.3 Boundary conditions

1) Continuity requirements

$$\left\{ \theta\Big|_{z^*=\left(\frac{L}{2}-l\right)^-} = \theta\Big|_{z^*=\left(\frac{L}{2}-l\right)^+},\ v\Big|_{z^*=\left(\frac{L}{2}-l\right)^-} = v\Big|_{z^*=\left(\frac{L}{2}-l\right)^+},\ u\Big|_{z^*=\left(\frac{L}{2}-l\right)^-} = u\Big|_{z^*=\left(\frac{L}{2}-l\right)^+} \right. \tag{27}$$

$$\left\{ \theta\Big|_{z^*=\left(\frac{L}{2}+l\right)^-} = \theta\Big|_{z^*=\left(\frac{L}{2}+l\right)^+},\ v\Big|_{z^*=\left(\frac{L}{2}+l\right)^-} = v\Big|_{z^*=\left(\frac{L}{2}+l\right)^+},\ u\Big|_{z^*=\left(\frac{L}{2}+l\right)^-} = u\Big|_{z^*=\left(\frac{L}{2}+l\right)^+} \right. \tag{28}$$

Substitution of expressions of displacement ($u$, $v$) and bending angle ($\theta$), as derived above, into Eqs. (27) and (28) leads to six equations, which include nine unknowns: $C_{11}$, $C_{12}$, $C_{13}$, $C_{21}$, $C_{22}$, $C_{23}$, $C_{31}$, $C_{32}$, and $C_{33}$.

Once the displacements at the segment ends are available, the corresponding reactions can be found by the following equations:

$$\begin{cases} H_0 = -k_{0h}\left(u\cos\varphi + v\sin\varphi\right)\Big|_{s=-R\Theta/2},\ V_0 = -k_{0v}\left(u\cos\varphi - v\sin\varphi\right)\Big|_{s=-R\Theta/2} \\ H_L = k_{Lh}\left(u\cos\varphi - v\sin\varphi\right)\Big|_{s=R\Theta/2},\ V_L = k_{Lv}\left(u\sin\varphi + v\cos\varphi\right)\Big|_{s=R\Theta/2} \\ M_0 = k_{0r}\theta\Big|_{s=-R\Theta/2},\ M_L = k_{Lr}\,\theta\Big|_{s=R\Theta/2} \end{cases} \tag{29}$$

where $H_L$ and $V_L$ are the horizontal and vertical reactions at the other (right) end, and $M_L$ is the corresponding bending moment.

2) Equilibrium condition of forces

The reactions on the tunnel lining segment must satisfy the equilibrium of forces, thus:

$$H_0 = H_L,\ V_0 + V_L = 2F,\ M_0 = M_L + V_L L - FL \tag{30}$$

Substituting Eqs. (29) and (30) into the corresponding equations of $u$ and $v$, these 12 unknowns: $C_{11}$, $C_{12}$, $C_{13}$, $C_{21}$, $C_{22}$, $C_{23}$, $C_{31}$, $C_{32}$, $C_{33}$, $H_0$, $V_0$, and $M_0$ can be obtained. Because of the large number of unknowns and couplings between them, it is cumbersome to solve these equations directly. In fact, re-organising the sequence of the solution can help uncouple some of the unknowns. After observation of these equations, it can be easily found that $C_{11}$,

$C_{12}$, $C_{13}$, $C_{31}$, $C_{32}$, and $C_{33}$ can be solved first, followed by $C_{21}$, $C_{22}$, and $C_{23}$; and then $H_0$, $V_0$, and $M_0$. When these unknowns are solved, the displacements and bending angle can be obtained directly with the substitution of solutions into corresponding equations.

## 2.4 Determination of transient temperature field

When the tunnel segment is subjected to a fire, the heat transfer can be represented by one side flow onto the concrete surface. In the tunnel longitudinal direction, the highest temperature decreases with the distance from the fire, which is usually influenced by the fire scale and the ventilation condition (the wind speed) (Shen, 2015; Yan, 2007). The temperature distributions along the tunnel longitudinal direction for specific fire scenarios were measured and analyzed by Yan (2007). Here, the temperature difference in the longitudinal direction is neglected since it plays a negligible role in the bending deflection (Shen, 2015).

When a reinforced concrete slab or beam is exposed to a standard fire (such as ISO834 and ASTM E119) from a single side, the temperature rise at different depths may be predicted through an empirical method (Kodur et al. 2013, Gao et al. 2014). In an underground space, the Eurocode HC fire is usually utilized. Accordingly, the temperature distribution along the depth of the segment can be determined by one-dimensional heat flow equations.

$$\frac{\partial\left(\lambda_c \frac{\partial T}{\partial y}\right)}{\partial y} = \rho c\left(T\right)\frac{\partial T}{\partial t} \tag{31}$$

where $\lambda_c$ is the heat conductivity coefficient of concrete; $\rho$ is the concrete density, which is assumed to remain unchanged (2400 Kg/m$^3$); $c\left(T\right)$ is heat capacity of concrete at temperature $T$.

In a practical situation, the inner side of the tunnel segment is exposed to heat, while the opposite side closely contacts with its surrounding soil. Therefore, the boundary conditions can be expressed as follows:

$$\begin{cases} -\lambda_c \dfrac{\partial T}{\partial \boldsymbol{n}} = \beta(T) \bullet (T - T_a), \text{ at the heated side} \\ T_c = T_s,\ \lambda_c \dfrac{\partial T_c}{\partial \boldsymbol{n}} = \lambda_s \dfrac{\partial T_s}{\partial \boldsymbol{n}}, \text{ at the cool side} \end{cases} \tag{32}$$

where $T_a$ is the temperature of the hot air; $\beta(T)$ is the heat exchange coefficient between the hot air and the concrete; $\lambda_s$ is the heat conductivity of soil, $\boldsymbol{n}$ is the normal vector at the boundary; $T_c$ and $T_s$ are the temperature of concrete and soil at the boundary, respectively.

A finite difference method can be adopted to calculate the temperature field (Guo and Shi, 2003; Ju and Zhang, 1998). The thermal parameters ($\beta(T)$, $\lambda_c$, $c(T)$) above can be taken from existing data (Guo and Shi, 2003). An explicit difference scheme has been employed in Guo and Shi (2003) to predict the temperature of concrete subjected to ISO 834 fire. In addition, temperature charts have been made available for concrete with different thicknesses. In the present model, the above method is adoped for the evaluation of the temperature field in the lining segment.

**2.5 Thermal damage of concrete**

The hydration products of cement mainly contain the calcium silicate hydrate (C-S-H) and calcium hydroxide (CH). Besides, there are also pores and unhydrated clinker in the cement paste (Zhang et al., 2017 and 2018). Under high temperature, C-S-H and CH will decompose. On the other hand, the aggregates may undergo crystal transition (siliceous aggregates) or decarbonation (calcareous aggregates). Therefore, the thermal degradation of concrete is generally induced by the damage of cement paste caused by thermal decomposition and thermal incompatibility, the deterioration of aggregates, and the interfacial damage between aggregates and the cement paste matrix (Lee et al., 2009; Zhao et al., 2012; Zhao et al., 2014). At the micro-scale, the decomposition of the constituents (C-S-H product and CH) of cement paste will lead to the loss of water. The loss of water is expected to increase the porosity of the reactant, which is the main mechanical degradation of cement paste (Zhao et al., 2014).

In order to take the effects of the mismatch between the deformations of cement paste and aggregates into consideration, Lee et al. (2009) used a function obtained from a regression curve from test data. Here, the process of derivation is omitted for simplicity. Finally, the thermal degree $d(T)$ of concrete can be expressed as follows:

For 120 □-400 □,

$$d(T)=1-\frac{\left(39.21\bullet 10^{-3}+e^{-0.002T}\right)\bullet\left(697.126\bullet 10^{-3}-253.828\bullet 10^{-6}T\right)}{651.437\bullet 10^{-3}+126.914\bullet 10^{-6}T} \tag{33}$$

For 400 □-530 □,

$$\begin{aligned} d(T)=1-&\frac{563.948\bullet 10^{4}\bullet\left(39.21\bullet 10^{-3}+e^{-0.002T}\right)\bullet\left(697.126\bullet 10^{-3}-253.828\bullet 10^{-6}T\right)}{\left(77.1825+T\right)\bullet\left(5132.91+T\right)} \\ &\bullet\left(178.434\bullet 10^{-2}-279.418\bullet 10^{-5}T\right) \end{aligned} \tag{34}$$

For 530 □-800 □,

$$d(T)=1-\frac{357.689\bullet 10^{-3}\bullet\left(39.21\bullet 10^{-3}+e^{-0.002T}\right)\bullet\left(697.126\bullet 10^{-3}-253.828\bullet 10^{-6}T\right)}{651.437\bullet 10^{-3}+126.914\bullet 10^{-6}T} \tag{35}$$

Apparently, the temperature is the only variable in the above three equations; however, the phase transformation and thermal incompatible damage are accounted for at the micro-scale. It should also be noted that these equations have been established based on the cement paste with a water/cement ratio of 0.67, but these equations can reproduce relatively good accuracy since the cement paste only accounts for a small volume (Zhao et al., 2014). As aforementioned, the deterioration of concrete also depends on the aggregate type. The above equations can be extended to other types of aggregates by modifying the terms in the first bracket based on test results. Detailed derivations can be found in Zhao et al. (2014).

# 3. Case study

## 3.1 General symmetric condition

In practical tunnel engineering, a symmetric design is usually adopted. When the support stiffness at both ends of a segment is the same or the difference can be neglected, the boundary conditions can be simplified as follows:

(1) Continuity condition:

$$\left\{ \theta\Big|_{z^*=\left(\frac{L}{2}-l\right)^-} = \theta\Big|_{z^*=\left(\frac{L}{2}-l\right)^+},\ v\Big|_{z^*=\left(\frac{L}{2}-l\right)^-} = v\Big|_{z^*=\left(\frac{L}{2}-l\right)^+},\ u\Big|_{z^*=\left(\frac{L}{2}-l\right)^-} = u\Big|_{z^*=\left(\frac{L}{2}-l\right)^+} \right. \tag{36}$$

(2) Boundary conditions at the end:

$$\begin{cases} H_0 = -k_{0h}\left(u\cos\varphi + v\sin\varphi\right)\big|_{s=-R\Theta/2} \\ V_0 = -k_{0v}\left(u\cos\varphi - v\sin\varphi\right)\big|_{s=-R\Theta/2} \\ M_0 = k_{0r}\theta\big|_{s=-R\Theta/2} \end{cases} \qquad \varphi = -\Theta/2, z^* = 0 \tag{37}$$

(3) Boundary conditions at the mid-span:

$$\theta\Big|_{z^*=\frac{L}{2}} = 0,\ u\Big|_{z^*=\frac{L}{2}} = 0,\ V_{\text{int}}\big|_{z^*=\frac{L}{2}} = 0,\ \ \varphi = 0, z^* = \frac{L}{2} \tag{38}$$

Substituting these boundary conditions into the corresponding equations, several unknowns can be determined as described below.

When $\theta|_{s=0} = 0$ $V_{\text{int}}|_{s=0} = 0$ is satisfied, we have $C_{21} = C' = 0$. For $u|_{s=0} = 0$, it can be fund that $C_{23}$=0. All the unknowns can be solved with the given symmetric boundary conditions. In the following sub-sections, some examples will be discussed as references for the fire-resistant design of tunnel lining segments.

### 3.2 Statically determinate case

In practical engineering, tunnel lining segments are usually designed to be statically indeterminate systems. However, analysis of a statically determinate case provides a lower-bound limit capacity for the lining segments, which is useful to assess the capacity when the boundary conditions are difficult to estimate.

As shown in **Fig.3**, the boundary conditions for a determinate segment will specialize as follows:

(1) The continuity condition remain the same as Eq. (36).

(2) The boundary condition at the segment ends can be simplified as:

$$\begin{cases} H_0 = N \\ \left(u\cos\varphi - v\sin\varphi\right)\big|_{s=-R\Theta/2} = 0 \quad \varphi = -\Theta/2, z^* = 0 \\ M_0 = 0 \end{cases} \tag{39}$$

(3) The condition at mid-span remain the same as Eq. (38).

In this case, $H_0$ is replaced by a known axial forxe $N$. The bending moment $M_0$ at the end equals zero. With a similar process of derivation as described in Section 3.1, all the unknowns in this boundary condition can be solved completely.

### 3.3 Tunnel lining segment with two hinged ends

The tunnel lining segment with two hinge ends is another special condition. From **Fig.4**, it can be seen that bending moments at both ends are zero. Other boundary conditions can be expressed as follows:

(1) The expression of continuity condition is the same as Eq. (36).

(2) The boundary condition at the end can be re-written as:

$$\begin{cases} \left(u\cos\varphi + v\sin\varphi\right)\Big|_{s=-R\Theta/2} = 0 \\ \left(u\cos\varphi - v\sin\varphi\right)\Big|_{s=-R\Theta/2} = 0 \quad \varphi = -\Theta/2, z^{*} = 0 \\ M_0 = 0 \end{cases} \tag{40}$$

(3) The condition at the mid-span can be expressed by Eq. (38).

Using the boundary conditions as described above, all the unknowns in the lining segment can be solved completely and the reaction forces at the ends can be obtained.

### 3.4 Tunnel lining segment with two fixed ends

Comparing with two types of boundary condition as described above, tunnel lining segment with two fixed ends shows a stiffer flexural stiffness (c.f. **Fig. 5**). The corresponding boundary conditions can be written as follows:

(1) Eq. (36) can be used to describe the continuity condition.

(2) The boundary condition at the end can be simplified as

$$\begin{cases} \left(u\cos\varphi + v\sin\varphi\right)\Big|_{s=-R\Theta/2} = 0 \\ \left(u\cos\varphi - v\sin\varphi\right)\Big|_{s=-R\Theta/2} = 0 \quad \varphi = -\Theta/2, \quad z^{*} = 0 \\ \theta\Big|_{s=-R\Theta/2} = 0 \end{cases} \tag{41}$$

(3) The condition at mid-span is the same as Eq. (38).

The tunnel lining segment can be solved accordingly.

## 4. Validation

### 4.1 Test specimens

Several experimental tests about tunnel lining segments with various boundary conditions were conducted to validate this proposed multilayer model. The specimens utilized in the tests were at about 1:3 scale to the actual size in real tunnel linings. Such a scale was determined so as to allow the composition of the materials as in the actual construction to be maintained in the test specimens to avoid the material scaling effect.

The dimensions of all the test specimens were 300-mm wide and 120-mm thick with an average radius of 990 mm. **Fig.6** shows the details of the specimens. All the specimens were cured for 28 days in the standard environment.

### 4.2 Test set-up and main measurements

The loading condition in a real shield TBM tunnel structure may be generally characterized by an inward pressure exerted by the surrounding soil. However, the actual distribution of the pressure load is complicated and could vary from segment to segment. In this test set-up, the mechanical loading and support conditions of the test segments were arranged so as to be representative of the corresponding conditions in a segment unit within a real shield tunnel lining structure, but in a simplified manner. In the experiment, the external pressure load was simplified into two-point loads applied vertically at the one-third span locations of the segment. Depending on the location of a specific segment within a tunnel shield ring, especially at the top and bottom regions, the midspan of the segment could be subjected to a positive moment (the inner side in tension). To represent the effect of such conditions under elevated temperature, selected specimens were preloaded to an initial positive moment condition.

The tests were carried out through a multi-function experimental system at Tongji University (see **Fig. 7**(a)). This system consists of a fire simulation subsystem powered by two combustors of industrial grade, a loading subsystem, and an auto-measurement and data acquisition subsystem. The fire simulation subsystem can achieve a desired heating-up history with the feedback of temperature in the furnace through a programmed control system. In addition, it can simulate the actual fire scenarios since the maximum temperature in the furnace can reach 1200 °C and the maximum heating rate is approximately 250 °C/min. The loading subsystem has been developed with a pair of adjustable supports, thus it can simulate different boundary conditions according to the requirements. The combination of these two subsystems makes it possible to investigate the response of tunnel lining segments under both applied mechanical loads and elevated temperatures.

LVDTs and K-type thermocouples were employed to measure the mid-span deflections and the temperature distribution through the cross-section of the segment specimens. Two measuring sections were arranged to measure the temperature within each test specimen, and at each measuring section five K-type thermocouples were installed, at the positions of 10 mm, 30 mm, 60 mm, 90 mm and 120 mm from the heating surface of the linings, respectively. In addition, a K-type thermocouple was installed on the extrados linings (120 mm from the heating surface). Aluminum powder with high heat conductivity was poured into the holes to ensure that the thermocouples and concrete contact closely. For the mechanical loading, a load cell was placed under each hydraulic actuator to control the level of the applied load (c.f. **Fig. 7**). The LVDTs for measuring displaceemnts were carefully protected from high temperature. More details of the experimental setup can be found in Yan et al. (2015).

As the horizontal support force represents the horizontal constraint on an individual segment as a boundary condition, two levels of such a boundary condition (BC) were employed, namely, a) BC1: no horizontal load, i.e. free sliding (lower bound); b) BC2: controlled horizontal load to maintain a no sliding condition. **Table 1** lists the detailed information about the load condition adopted in this present study, as well as the corresponding boundary conditions. Specifically, two load cases are considered in this study, namely:

(1) Loading Case1 (LC-1): In this case, the test segments were first loaded mechanically to a prescribed initial (service) load level, and then subjected to a complete heating (following the standard Eurocode HC curve (CEN, 2004)) and cooling period. After complete

cooling, the specimens were loaded to the onset of visible concrete cracking by increasing the vertical load, to investigate the mechanical behavior after exposure to high temperature. Two pairs of specimens were tested with LC-1, under two different boundary conditions, respectively, including RC5 (under BC1); RC4 (under BC2).

(2) Loading Case2 (LC-2): The specimens were heated following the standard Eurocode HC curve, without any initial loads. After approximately 40 min of heating, the specimens were mechanically loaded to the onset of visible concrete cracking to investigate the response under elevated temperatures. One specimen was subjected to the LC-2 test (RC1 under BC1).

### 4.3 Test results and discussions

The standard Eurocode HC curve, which was adopted to simulate the small oil fire in the test, can be written as:

$$T = 20 + 1080(1 - 0.325e^{-0.167t} - 0.675e^{-2.5t}) \tag{42}$$

where $t$ is the time (in minutes) and $T$ is the gas temperature in the furnace at time $t$. The actual temperature in the furnace measured in the tests is shown in **Fig.7 (b)**, along with the values calculated by Eq. (42). It can be seen from this figure that the fire simulation system can well resemble the standard HC curve. In addition, the measured temperature distributions through the cross-section at different heating time are shown in **Fig.8**. This figure indicates that the temperature gradient of the temperature field intensifies with the heating time.

The accuracy of the multilayer model described in Section 3 can be improved through increasing the number of the layers according to the characteristics of the actual tunnel lining segment. The degradation of the Young's modulus of steel bar under different temperature can be estimated through an empirical expression:

$$d_s(T) = 1 - \left(1.03 + 7(T-20)^6 \times 10^{-7}\right)^{-1}, \text{ under fire} \tag{43}$$

$$d_s\left(T\right)=0.0011+0.0249T/100\text{, post fire} \tag{44}$$

The constitutive relations of concrete under different temperature, as given in CEN (2004), are approximately illustrated in **Fig. 9**. From this figure, it can be seen that the compressive stress-strain relation of concrete under different temperature are reasonably linear. Therefore, the linear stress-strain relationship is considered in this study. The damage of concrete also has significant effects on the deformation of the specimens (Sun and Li, 2016; Ding and Li, 2017; Li and Wu, 2018; Suchorzewski, 2018). The damage evolution of concrete with temperature can be determined through Eqs. (33) – (35), which is shown in **Fig. 10**. When the temperature is beyond 800 °C, the damage degree of concrete will reach 100%. The reduction rate of elasticity modulus will reach 1/6 of the value in ambient from 100°C to 900°C. From other experiment results (Lee et al., 2009; Zhao et al., 2012; Zhao et al., 2014), taking into account the effects of thermal decomposition and microcracking of heated cement paste, the Young's modulus has also been found to reduce by 70% to 80% when temperature increases from 100°C to 600°C.

The temperature of the specimen measured during the test is regarded as the input of the present multilayer model. The properties of concrete after a fire are assessed based on the highest temperature recorded, while the properties of steel bar after fire recover to the unheated properties (Chen and Liu, 2004; Haddad and Shannis, 2004).

The displacements at the mid-span of these specimens are calculated by the multilayer model. The predicted results and test results are compared in **Figs. 11-13**. **Fig. 11** shows the results of the statically determinate specimen (RC1) under elevated temperatures. **Fig. 12** shows the load-displacement at mid-span of RC5 after cooling. For specimen RC 4 with two fixed ends, the load-displacement curve is shown in **Fig. 13**.

Compared with the segments after fire exposure, the segment under fire exhibits a higher bending stiffness by approximately 2.0 times. From other experiments (Yan et al., 2012; Yan et al., 2013), the segment under fire has also been observed to exhibit 1.5~3 times the bending stiffness of the segments in a post-fire condition. Furthermore, segments under more restricted boundary conditions can improve the ultimate bearing capacity by as much as 5 times or even more. All the predicted results compare well with the test results, indicating that this model is suitable for the calculation of the response of tunnel lining segments under elevated temperature.

It should be noted that the loading condition adopted in the present analysis of the behavior of tunnel lining segments under fire is a simplified case with concentrated loads. In practical engineering, the main load may be a uniformly distributed load, and in some special cases a combination of concentrated and uniform distributed loads may appear, such as in the case of a eccentric terrene heaped load and ground water seepage. For a uniformly distributed load, a similar derivation can be carried out, and the internal force at any section of the tunnel lining segment can be rewritten as:

$$\text{Bending moment: } M_{\text{int}} = M_0 - H_0 y^* + V_0 z^* - \frac{1}{2} q z^{*2} \tag{45}$$

$$\text{Axial thrust: } N_{\text{int}} = H_0 \cos\varphi + V_0 \sin\varphi - q z^* \sin\varphi \tag{46}$$

$$\text{Shear force: } V_{\text{int}} = H_0 \sin\varphi - V_0 \cos\varphi + q z^* \cos\varphi \tag{47}$$

Using a given boundary condition, the solution can be derived in a standard process. The response of the tunnel lining segment under a combination of concentrated and uniformly distributed loads can be obtained through the superposition of responses under each load pattern.

The model also has limitations. The stress-strain model and the layering strategy of the segment section require rational match-up to reduce the calculation cost and improve the result accuracy. On the other hand, the lining segments linked by segmental joints my exhibit more sophisticated behavior as general boundary conditions, and modelling such boundary conditions will require a more suitbale joint model. Further development is also required to extend the multilayer segment model for the analysis of the entire ring structure.

# 5. Conclusions

A multilayer thermo-elastic damage model for bending deflection of the tunnel lining segment exposed to fire is developed. The key features of the model and the main conclusions may be summarized as follows:

(1) The basic unknowns are the tangential and radial displacement of a tunnel lining segment in the proposed model. Based on the plane cross-section assumption, the cross-section is divided into multilayers and the strain distribution over the section is derived. In accordance with the geometric relation between the displacement and strain, it leads to the general solution of the radial and tangential displacements of the tunnel lining segment with 9 integration constants. Combining the continuity and force equilibrium conditions, equations are established to solve 12 basic unknown parameters.

(2) A multi-scale thermal damage model is introduced to describe the damage evolution of the tunnel segment in fire. When the temperature is beyond 800 °C, the damage degree of concrete is assumed to reach 100%. The reduction rate of the elasticity modulus reaches 1/6 of the value in ambient from 100°C to 900°C. Examples with typical boundary conditions, such as a statically determinate segment, a statically indeterminate lining segment with two hinged ends, and a lining segment with fixed ends, are given to illustrate the working of this multilayer model.

(3) The accuracy of the proposed model is verified by comparing the predictions with experimental results from four-point bending tests under and after the fire. The comparisions demonstrate that this model is capable of analyzing the response of tunnel lining segment

under non-uniform temperature field with satisfactory accuracy. Both the experimental and the analytical results indicate that a restricted boundary condition can improve the ultimate bearing capacity of the lining segment by as much as five times or even more.

## Acknowledgments

The authors acknowledge the financial supports from the National Natural Science Foundation of China (51578410, 51478345), Shanghai Natural Science Foundation (17DZ1203804), and the Research Fund of State Key Laboratory for Disaster Reduction in Civil Engineering (SLDRCE19-A-14). Furthermore, authors are deeply thankful to Jinan Yellow River Tunnel Research Project to support this study.

## Appendix

$$\lambda = \frac{\sum_{\alpha=1}^{n} \overline{(EA)_\alpha}}{\left(\sum_{\alpha=1}^{n} \overline{(EA)_\alpha}\right)\left(\sum_{\alpha=1}^{n} \overline{(EI)_\alpha}\right) - \left(\sum_{\alpha=1}^{n} \overline{(EB)_\alpha}\right)^2} \tag{A1}$$

$$A = M_0 + M_\Pi - \frac{\sum_{\alpha=1}^{n} \overline{(EB)_\alpha}}{\sum_{\alpha=1}^{n} \overline{(EA)_\alpha}} N_\Pi + H_0 R \cos\left(\frac{\Theta}{2}\right) + V_0 R \sin\left(\frac{\Theta}{2}\right) \tag{A2}$$

$$B = -H_0 R \left( R + \frac{\sum_{\alpha=1}^{n} \overline{(EB)_\alpha}}{\sum_{\alpha=1}^{n} \overline{(EA)_\alpha}} \right) \tag{A3}$$

$$C = V_0 R \left( -R + \frac{\sum_{\alpha=1}^{n} \overline{(EB)_\alpha}}{\sum_{\alpha=1}^{n} \overline{(EA)_\alpha}} \right) \tag{A4}$$

$$A' = M_0 + M_\Pi - \frac{\sum_{\alpha=1}^{n} \overline{(EB)_\alpha}}{\sum_{\alpha=1}^{n} \overline{(EA)_\alpha}} N_\Pi + H_0 R \cos\left(\frac{\Theta}{2}\right) + V_0 R \sin\left(\frac{\Theta}{2}\right) - FR \sin\left(\frac{\Theta}{2}\right) - F\left(l - \frac{L}{2}\right) \tag{A5}$$

$$C' = \left(V_0 - F\right) R \left( -R + \frac{\sum_{\alpha=1}^{n} \overline{(EB)_\alpha}}{\sum_{\alpha=1}^{n} \overline{(EA)_\alpha}} \right) \tag{A6}$$

$$A'' = M_0 + M_\Pi - \frac{\sum_{\alpha=1}^{n} \overline{(EB)_\alpha}}{\sum_{\alpha=1}^{n} \overline{(EA)_\alpha}} N_\Pi + H_0 R \cos\left(\frac{\Theta}{2}\right) + V_0 R \sin\left(\frac{\Theta}{2}\right) - 2Fl \tag{A7}$$

$$C'' = R \left[ -V_0 R + \frac{\sum_{\alpha=1}^{n} \overline{(EB)_\alpha}}{\sum_{\alpha=1}^{n} \overline{(EA)_\alpha}} \left(V_0 - 2F\right) \right] \tag{A8}$$

$$\theta = \lambda \left\{ \begin{aligned} & M_0 s + M_\Pi s - \frac{\sum_{\alpha=1}^{n} \overline{(EB)_\alpha}}{\sum_{\alpha=1}^{n} \overline{(EA)_\alpha}} N_\Pi s - H_0 \left[ \left( R + \frac{\sum_{\alpha=1}^{n} \overline{(EB)_\alpha}}{\sum_{\alpha=1}^{n} \overline{(EA)_\alpha}} \right) R \sin\varphi - Rs \cos\left(\frac{\Theta}{2}\right) \right] \\ & + V_0 R \left[ s \sin\left(\frac{\Theta}{2}\right) + \left( \frac{\sum_{\alpha=1}^{n} \overline{(EB)_\alpha}}{\sum_{\alpha=1}^{n} \overline{(EA)_\alpha}} - R \right) \cos\varphi \right] \end{aligned} \right\} + C_{11} \tag{B1}$$

$$v = \lambda \left\{ \begin{aligned} & \frac{M_0 s^2}{2} + \frac{M_\Pi s^2}{2} - \frac{\sum_{\alpha=1}^{n} \overline{(EB)_\alpha}}{\sum_{\alpha=1}^{n} \overline{(EA)_\alpha}} \frac{N_\Pi s^2}{2} + H_0 R \left[ \begin{aligned} & \left( R + \frac{\sum_{\alpha=1}^{n} \overline{(EB)_\alpha}}{\sum_{\alpha=1}^{n} \overline{(EA)_\alpha}} \right) R \cos\varphi \\ & + \frac{s^2}{2} \cos\left(\frac{\Theta}{2}\right) \end{aligned} \right] \\ & + V_0 R \left[ \frac{s^2}{2} \sin\left(\frac{\Theta}{2}\right) + R \left( \frac{\sum_{\alpha=1}^{n} \overline{(EB)_\alpha}}{\sum_{\alpha=1}^{n} \overline{(EA)_\alpha}} - R \right) \sin\varphi \right] \end{aligned} \right\} + C_{11} s + C_{12} \tag{B2}$$

For $\frac{L}{2} - l < z^* \le \frac{L}{2} + l$,

$$\theta=\lambda\left\{\begin{aligned}&M_0 s+M_\Pi s-\frac{\sum_{\alpha=1}^{n}\overline{(EB)_\alpha}}{\sum_{\alpha=1}^{n}\overline{(EA)_\alpha}}N_\Pi s-H_0\left[\left(R+\frac{\sum_{\alpha=1}^{n}\overline{(EB)_\alpha}}{\sum_{\alpha=1}^{n}\overline{(EA)_\alpha}}\right)R\sin\varphi-Rs\cos\left(\frac{\Theta}{2}\right)\right]\\&+V_0R\left[s\sin\left(\frac{\Theta}{2}\right)+\left(\frac{\sum_{\alpha=1}^{n}\overline{(EB)_\alpha}}{\sum_{\alpha=1}^{n}\overline{(EA)_\alpha}}-R\right)\cos\varphi\right]-F\left(l-\frac{L}{2}\right)s-FR\left[s\sin\left(\frac{\Theta}{2}\right)+\left(\frac{\sum_{\alpha=1}^{n}\overline{(EB)_\alpha}}{\sum_{\alpha=1}^{n}\overline{(EA)_\alpha}}-R\right)\cos\varphi\right]\end{aligned}\right\}+C_{21}\qquad\text{(B3)}$$

$$v=\lambda\left\{\begin{aligned}&-\frac{\sum_{\alpha=1}^{n}\overline{(EB)_\alpha}}{\sum_{\alpha=1}^{n}\overline{(EA)_\alpha}}\frac{N_\Pi s^2}{2}+H_0R\left[\left(R+\frac{\sum_{\alpha=1}^{n}\overline{(EB)_\alpha}}{\sum_{\alpha=1}^{n}\overline{(EA)_\alpha}}\right)R\cos\varphi+\frac{s^2}{2}\cos\left(\frac{\Theta}{2}\right)\right]\\&\frac{M_0s^2}{2}+\frac{M_\Pi s^2}{2}+V_0R\left[\frac{s^2}{2}\sin\left(\frac{\Theta}{2}\right)+R\left(\frac{\sum_{\alpha=1}^{n}\overline{(EB)_\alpha}}{\sum_{\alpha=1}^{n}\overline{(EA)_\alpha}}-R\right)\sin\varphi\right]\\&-FR\left[\frac{s^2}{2}\sin\left(\frac{\Theta}{2}\right)+R\left(\frac{\sum_{\alpha=1}^{n}\overline{(EB)_\alpha}}{\sum_{\alpha=1}^{n}\overline{(EA)_\alpha}}-R\right)\sin\varphi\right]-F\frac{s^2}{2}\left(l-\frac{L}{2}\right)\end{aligned}\right\}+C_{21}s+C_{22}\qquad\text{(B4)}$$

For $z^*>\frac{L}{2}+l$,

$$\theta=\lambda\left\{\begin{aligned}&M_0 s+M_\Pi s-\frac{\sum_{\alpha=1}^{n}\overline{(EB)_\alpha}}{\sum_{\alpha=1}^{n}\overline{(EA)_\alpha}}N_\Pi s-H_0\left[\left(R+\frac{\sum_{\alpha=1}^{n}\overline{(EB)_\alpha}}{\sum_{\alpha=1}^{n}\overline{(EA)_\alpha}}\right)R\sin\varphi-Rs\cos\left(\frac{\Theta}{2}\right)\right]\\&+V_0R\left[s\sin\left(\frac{\Theta}{2}\right)+\left(\frac{\sum_{\alpha=1}^{n}\overline{EB_\alpha}}{\sum_{\alpha=1}^{n}\overline{EA_\alpha}}-R\right)\cos\varphi\right]-2F\left(ls+R\frac{\sum_{\alpha=1}^{n}\overline{(EB)_\alpha}}{\sum_{\alpha=1}^{n}\overline{(EA)_\alpha}}\cos\varphi\right)\end{aligned}\right\}+C_{31}\qquad\text{(B5)}$$

$$v=\lambda\left\{\begin{aligned}&\frac{M_0s^2}{2}+\frac{M_\Pi s^2}{2}-\frac{\sum_{\alpha=1}^{n}\overline{(EB)_\alpha}}{\sum_{\alpha=1}^{n}\overline{(EA)_\alpha}}\frac{N_\Pi s^2}{2}-2F\left(\frac{1}{2}ls^2+R^2\frac{\sum_{\alpha=1}^{n}\overline{(EB)_\alpha}}{\sum_{\alpha=1}^{n}\overline{(EA)_\alpha}}\sin\varphi\right)\\&+H_0R\left[\left(R+\frac{\sum_{\alpha=1}^{n}\overline{(EB)_\alpha}}{\sum_{\alpha=1}^{n}\overline{(EA)_\alpha}}\right)R\cos\varphi+\frac{s^2}{2}\cos\left(\frac{\Theta}{2}\right)\right]+V_0R\left[\frac{s^2}{2}\sin\left(\frac{\Theta}{2}\right)+R\left(\frac{\sum_{\alpha=1}^{n}\overline{(EB)_\alpha}}{\sum_{\alpha=1}^{n}\overline{(EA)_\alpha}}-R\right)\sin\varphi\right]\end{aligned}\right\}+C_{31}s+C_{32}\qquad\text{(B6)}$$

If $z^*\le\frac{L}{2}-l$ and $N_{\text{int}}=H_0\cos\varphi+V_0\sin\varphi$:

$$u(s)=\frac{H_0R\sin\varphi-V_0R\cos\varphi+N_\Pi s}{\sum_{\alpha=1}^{n}\overline{EA_\alpha}}-\frac{\sum_{\alpha=1}^{n}\overline{(EB)_\alpha}}{\sum_{\alpha=1}^{n}\overline{(EA)_\alpha}}\theta \tag{C1}$$
$$+\int\frac{v}{R}ds-\int\frac{1}{2}\left(\frac{dv}{ds}\right)^2ds+C_{13}$$

where $\int\frac{v}{R}ds$ can be written as:

$$\int\frac{v}{R}ds=\frac{\lambda\left(\frac{As^3}{6}-BR\sin\varphi-CR\cos\varphi\right)+\frac{1}{2}C_{11}s^2+C_{12}s}{R} \tag{C2}$$

$$\int\frac{1}{2}\left(\frac{dv}{ds}\right)^2ds=\lambda^2\left[\begin{array}{l}\frac{1}{6}A^2s^3+\left(\frac{1}{4}B^2-ABR\cos\varphi+\frac{1}{4}C^2+ACR\sin\varphi\right)s\\+ACR^2\cos\varphi-\frac{1}{4}BCR^2\cos2\varphi-\frac{1}{8}\left(B^2-C^2\right)R\sin2\varphi+ABR^2\sin\varphi\end{array}\right] \tag{C3}$$
$$+\lambda C_{11}\left(\frac{As^2}{2}+C\sin\varphi-B\cos\varphi\right)+\frac{C_{11}^2s}{2}$$

For $z^*\le\frac{L}{2}-l$,

$$u(s)=\frac{H_0R\sin\varphi-V_0R\cos\varphi+N_\Pi s}{\sum_{\alpha=1}^{n}\overline{(EA)_\alpha}}-\frac{\sum_{\alpha=1}^{n}\overline{(EB)_\alpha}}{\sum_{\alpha=1}^{n}\overline{(EA)_\alpha}}\theta+\int\frac{v}{R}ds-\int\frac{1}{2}\left(\frac{dv}{ds}\right)^2ds+C_{13} \tag{C4}$$

For $\frac{L}{2}-l<z^*\le\frac{L}{2}+l$,

$$u(s)=\frac{H_0R\sin\varphi-V_0R\cos\varphi+FR\cos\varphi+N_\Pi s}{\sum_{\alpha=1}^{n}\overline{(EA)_\alpha}}-\frac{\sum_{\alpha=1}^{n}\overline{(EB)_\alpha}}{\sum_{\alpha=1}^{n}\overline{(EA)_\alpha}}\theta+\int\frac{v}{R}ds-\int\frac{1}{2}\left(\frac{dv}{ds}\right)^2ds+C_{23} \tag{C5}$$

$$\int\frac{v}{R}ds=\frac{\lambda\left(\frac{A's^3}{6}-BR\sin\varphi-C'R\cos\varphi\right)+\frac{1}{2}C_{21}s^2+C_{22}s}{R} \tag{C6}$$

$$\int \frac{1}{2}\left(\frac{dv}{ds}\right)^2 ds = \lambda^2 \left[\begin{array}{l} A'C'R^2\cos\varphi + \left(\frac{1}{4}B^2 - A'BR\cos\varphi + \frac{1}{4}C'^2 + A'C'R\sin\varphi\right)s \\ +\frac{1}{6}A'^2 s^3 - \frac{1}{4}BC'R^2\cos 2\varphi - \frac{1}{8}\left(B^2 - C'^2\right)R\sin 2\varphi + A'BR^2\sin\varphi \end{array}\right] + \lambda C_{21}\left(\frac{As^2}{2} + C'\sin\varphi - B\cos\varphi\right) + \frac{C_{21}^2 s}{2} \quad \text{(C7)}$$

For $z^* > \frac{L}{2} + l$ ,

$$u(s) = \frac{H_0 R\sin\varphi - V_0 R\cos\varphi + 2FR\cos\varphi + N_\Pi s}{\sum_{\alpha=1}^{n}\overline{(EA)_\alpha}} - \frac{\sum_{\alpha=1}^{n}\overline{(EB)_\alpha}}{\sum_{\alpha=1}^{n}\overline{(EA)_\alpha}}\theta + \int \frac{v}{R}ds - \int \frac{1}{2}\left(\frac{dv}{ds}\right)^2 ds + C_{33} \quad \text{(C8)}$$

$$\int \frac{v}{R}ds = \frac{\lambda\left(\frac{A''s^3}{6} - BR\sin\varphi - C''R\cos\varphi\right) + \frac{1}{2}C_{31}s^2 + C_{32}s}{R} \quad \text{(C9)}$$

$$\int \frac{1}{2}\left(\frac{dv}{ds}\right)^2 ds = \lambda^2 \left[\begin{array}{l} \frac{1}{6}A''^2 s^3 + \left(\frac{1}{4}B^2 - A''BR\cos\varphi + \frac{1}{4}C''^2 + A''C''R\sin\varphi\right)s \\ +A''C''R^2\cos\varphi - \frac{1}{4}BC''R^2\cos 2\varphi - \frac{1}{8}\left(B^2 - C''^2\right)R\sin 2\varphi + A''BR^2\sin\varphi \end{array}\right] + \lambda C_{31}\left(\frac{As^2}{2} + C'\sin\varphi - B\cos\varphi\right) + \frac{C_{31}^2 s}{2} \quad \text{(C10)}$$

It should be noted that *A*, *B*, *C*, *A'*, *C'*, *A''*, and *C''* are displayed in the Eqs. (A2)- (A8), respectively.

# References


Bangi, M. R., and Horiguchi, T., 2012. Effect of fibre type and geometry on maximum pore pressures in fibre-reinforced high strength concrete at elevated temperatures. Cement and Concrete Research, 42(2), 459-466.

Bažant, Z.P., 1997. Analysis of pore pressure, thermal stress and fracture in rapidly heated concrete. Proceedings of the international workshop on fire performance of high strength concrete, NIST SP 919, pp. 155-164, Gaithersburg, Md, USA, 1997.

Beard, A.N., 2009. Fire safety in tunnels. Fire Safety J. 44, 276-278.

Blom C.B.M., 2002. Design philosophy of concrete linings for tunnels in soft soils. Delft

University Press.

Bradford, M. A., 2006. In-plane nonlinear behaviour of circular pinned arches with elastic restraints under thermal loading. International Journal of Structural Stability and Dynamics, 06(2), 163-177.

Bradford, M. A., 2010. Long-span shallow steel arches subjected to fire loading. Advances in Structural Engineering, 13(3), 501-511.

Chen, B., and Liu, J., 2004. Residual strength of hybrid-fiber-reinforced high-strength concrete after exposure to high temperatures. Cement and Concrete Research, 34(6), 1065-1069.

Chen, S.C., Lu, X.Z., Ren A.Z. and Jiang, J.J., 2009. Fiber beam model of concrete structure under fire. Chinese Journal of Computational Mechanics, 26(1), 72-79.

Chen, S.C., Ren A.Z., 2011. Structural failure mode analysis based on the fiber beam model and layered shell model. Journal of applied foundation and engineering science, 19(2), 260-270.

Choi, Soon-Wook, Lee, Junhwan, and Chang, Soo-Ho., 2013. A holistic numerical approach to simulating the thermal and mechanical behaviour of a tunnel lining subject to fire. Tunnelling and Underground Space Technology incorporating Trenchless Technology Research, 35(35), 122-134.

Ding, Z., and Li, J., 2017. A physically motivated model for fatigue damage of concrete. International Journal of Damage Mechanics, 27(8), 1192-1212.

European Committee for Standardization (CEN)., 2004. Eurocode 2: Design of concrete structures, EN 1992-1-2.

Gao, W. Y., Dai, J. G. and Teng, J. G., 2014. Simple Method for Predicting Temperatures in Reinforced Concrete Beams Exposed to a Standard Fire. Journal of Composites for Construction, 17(4), 573-589.

Gawin, D., Pesavento, F., and Schrefler, B.A., 2003. Modelling of hygro-thermal behaviour of concrete at high temperature with thermo-chemical and mechanical material degradation. Computer Methods in Applied Mechanics and Engineering, 192(13-14), 1731-1771.

Gawin, D., Pesavento, F., and Schrefler, B.A., 2006. Towards prediction of the thermal spalling risk through a multi-phase porous media model of concrete. Computer Methods in Applied Mechanics and Engineering, 195(41-43), 5707-5729.

Gawin, D., Pesavento, F., and Schrefler, B.A., 2010. Simulation of damage–permeability coupling in hygro-thermo-mechanical analysis of concrete at high temperature. Communications in Numerical Methods in Engineering, 18(2), 113-119.

Gandit, M., Kouabenan, D.R., Caroly, S., 2009. Road-tunnel fires: Risk perception and management strategies among users. Safety Science. 47, 105-114.

Guo, Z.H., Shi, X.D., 2003. High temperature performance of reinforced concrete and its calculation. Beijing, Tsinghua University Press.

Haddad, R. H., and Shannis, L. G., 2004. Post-fire behavior of bond between high strength pozzolanic concrete and reinforcing steel. Construction and Building Materials, 18(6), 425-435.

Han, H. T., Zhang, Z., and Lu, Z.X., 2010. Analytical method on bending of composite laminated beams with delaminations. Ald Mahma and Mhan, 31(07), 843-852.

Heidarpour, A., Abdullah, A. A., and Bradford, M. A., 2010a. Non-linear thermoelastic analysis of steel arch members subjected to fire. Fire Safety Journal, 45(3), 183-192.

Heidarpour, A., Abdullah, A. A., and Bradford, M. A., 2010b. Non-linear inelastic analysis of steel arches at elevated temperatures. Steel Construction, 66(4), 512-519.

Heidarpour, A. and Bradford, M. A., 2009. Generic nonlinear modelling of restrained steel beams at elevated temperatures. Engineering Structures, 31(11), 2787-2796.

Heidarpour, A., Pham, T. H., and Bradford, M. A., 2010c. Nonlinear thermoelastic analysis of composite steel–concrete arches including partial interaction and elevated temperature loading. Engineering Structures, 32(10), 3248-3257.

Huang, Z. R., Zhu, W., Liang, J. H., Lin, J., and Jia, R., 2006. Three-dimensional numerical modelling of shield tunnel lining. Tunnelling and Underground Space Technology, 21(3), 434-434.

Ibañez, C., Romero, M. L., and Hospitaler, A., 2013. Fiber beam model for fire response simulation of axially loaded concrete filled tubular columns. Engineering Structures, 56(6), 182-193.

Jiang, J.J., Lu, X.Z., 2013. Concrete structure finite element analysis. Tsinghua University Press.

Ju, J. W., Zhang, Y., 1998. Axisymmetric thermomechanical constitutive and damage modeling for airfield concrete pavement under transient high temperature. Mechanics of Materials, 29(3-4), 307-323.

Kalifa, P., Chéné, G., and Gallé, C., 2001. High-temperature behaviour of hpc with polypropylene fibres: from spalling to microstructure. Cement and Concrete Research, 31(10), 1487-1499.

Kalifa, P., Menneteau, F. D., and Quenard, D., 2000. Spalling and pore pressure in hpc at high temperatures. Cement and Concrete Research, 30(12), 1915-1927.

Klappers, C., Grübl, F., and Ostermeier, B., 2006. Structural analyses of segmental lining -coupled beam and spring analyses versus 3d-fem calculations with shell elements. Tunnelling and Underground Space Technology, 21(3-4), 254-255.

Kodur, V. K. R., and Sultan, M. A., 2003. Effect of temperature on thermal properties of high-strength concrete. Journal of Materials in Civil Engineering, 15(2), 101-107.

Kodur, V. K. R., and Yu, B., 2013. Evaluating the fire response of concrete beams strengthened with near-surface-mounted frp reinforcement. Journal of Composites for Construction, 17(4), 517-529.

Kodur, V. K. R., Yu, B. and Dwaikat, M. M. S., 2013. A simplified approach for predicting temperature in reinforced concrete members exposed to standard fire. Fire Safety Journal, 56(1), 39-51.

Kodur, V. R., Mcgrath, R. C., Leroux, P., and Latour, J. C., 2005. Experimental studies for evaluating the fire endurance of high-strength concrete columns. Research Report NRC Institute for Research in Construction.

Kodur, V., 2014. Properties of concrete at elevated temperatures. Isrn Civil Engineering, 2014, 1-15.

Koyama, Y., 2003. Present status and technology of shield tunneling method in japan. Tunnelling and Underground Space Technology, 18(2), 145-159.

Lee, J., Xi, Y., Willam, K., and Jung, Y., 2009. A multiscale model for modulus of elasticity of

concrete at high temperatures. Cement and Concrete Research, 39(9), 754-762.
Li, H., and Liu, G., 2016. Tensile properties of hybrid fiber-reinforced reactive powder concrete after exposure to elevated temperatures. International Journal of Concrete Structures and Materials, 10(1), 29-37.
Li, J.H., 2007. Research of calculation about the high temperature limit bearing capacity and the design method of fire resistance of reinforced concrete beam. Doctoral dissertation, Central South University.
Li, S. R., and Zhou, F. X., 2008. Geometrically nonlinear model and numerical simulation of elastic curved beams subjected to mechanical and thermal loads. Chinese Journal of Computational Mechanics, 25(1), 25-28.
Li, W. S. and Wu, J. Y., 2018. A consistent and efficient localized damage model for concrete, International Journal of Damage Mechanics, 27(4): 541-567.
Li, X. J., Yan, Z. G., Wang, Z., and Zhu, H. H., 2015. A progressive model to simulate the full mechanical behavior of concrete segmental lining longitudinal joints. Engineering Structures, 93, 97-113.
Liao, Z.C., 2011. The bearing capacity of the tunnel lining structure under fire research. Doctoral dissertation, Central South University.
Liu, X., Bai, Y., Yuan, Y., and Mang, H. A., 2014. Experimental investigation of the ultimate bearing capacity of continuously jointed segmental tunnel linings. Structure and Infrastructure Engineering, 12(10), 1-16.
Lv T. G., 1996. Experimental investigation on strength and deformation of steel bars at elevated temperature. Master thesis, Tsinghua University.
Mindeguia, J. C., Pimienta, P., Noumowé, A., and Kanema, M., 2010. Temperature, pore pressure and mass variation of concrete subjected to high temperature-experimental and numerical discussion on spalling risk. Cement and Concrete Research, 40(3), 477-487.
Molins, C., and Arnau, O., 2011. Experimental and analytical study of the structural response of segmental tunnel linings based on an in situ, loading test.: Part 1: test configuration and execution. Tunnelling and Underground Space Technology, 26(6), 764-777.
Nilsson, D., Johansson, M., Frantzich, H., 2009. Evacuation experiment in a road tunnel: A study of human behaviour and technical installations. Fire Safety Journal. 44, 458-468.
Phan, L. T., Lawson, J. R., and Davis, F. L., 2001. Effects of elevated temperature exposure on heating characteristics, spalling, and residual properties of high performance concrete. Materials and Structures, 34(2), 83-91.
Ružić, D., Kolšek, J., Planinc, I., Saje, M., and Hozjan, T., 2015. Non-linear fire analysis of restrained curved rc beams. Engineering Structures, 84, 130-139.
Schrefler, B. A., Pesavento, F., and Gawin, D., 2014. Multiphase Porous Media, High Temperature. Springer Netherlands.
Shen, Y., 2015. Research on thermo-mechanical coupled behavior of shield tunnel lining structure in fire. Doctoral dissertation, Tongji University.
Shen, Y., Yan, Z. G., and Zhu, H. H., 2015. An analytical mechanical model for tunnel segmental joints subjected to elevated temperatures. International Symposium on Systematic Approaches to Environmental Sustainability in Transportation.
Suchorzewski, J., Tejchman, J. and Nitka, M., 2018. Discrete element method simulations of fracture in concrete under uniaxial compression based on its real internal structure,

International Journal of Damage Mechanics, 27(4): 578-607.
Sun, B., and Li, Z., 2016. Adaptive concurrent three-level multiscale simulation for trans-scale process from material mesodamage to structural failure of concrete structures. International Journal of Damage Mechanics, 25(5), 750-769
Tang, F., Cao, Z. L., Chen, Q., Meng, N., Wang, Q., Fan, C. G., 2017a. Effect of blockage-heat source distance on maximum temperature of buoyancy-induced smoke flow beneath ceiling in a longitudinal ventilated tunnel. International Journal of Heat and Mass Transfer, 109, 683-688.
Tang, F., Mei, F.Z., Wang, Q., He, Z., Fan, C.G., Tao, C.F., 2017b. Maximum temperature beneath the ceiling in tunnel fires with combination of ceiling mechanical smoke extraction and longitudinal ventilation, Tunnelling and Underground Space Technology, 68:231-237.
Ulm, F. J., Acker, P., and LéVy, M., 1999b. The "chunnel" fire. ii: analysis of concrete damage. Journal of Engineering Mechanics, 125(3), 283-289.
Ulm, F. J., Coussy, O., and BažAnt, Z. P., 1999a. The "chunnel" fire. i: chemoplastic softening in rapidly heated concrete. Journal of Engineering Mechanics, 125(3), 272-282.
Vuilleumier, F., Weatherill, A., Crausaz, B., 2002. Safety aspects of railway and road tunnel: Example of the Lötschberg Railway Tunnel and Mont-Blanc Road Tunnel. Tunnelling and Underground Space Technology. 17(2), 153-158.
Wang, H., 2014. Analysis of fire scenario and the temperature field distribution of subway interval tunnel segments. Master dissertation, Nanjing University.
Wang, Q.Z., Meng, Q.C., 1998. Composite laminated beam delamination problem analytic solution. Journal of Beijing University of Aeronautics and Astronautics (3), 319-322.
Xiao, J., and König, G., 2004. Study on concrete at high temperature in China—an overview. Fire Safety Journal, 39(1), 89-103.
Yan, Z. G., Shen, Y., Zhu, H. H., and Lu, Y., 2016. Experimental study of tunnel segmental joints subjected to elevated temperature. Tunnelling and Underground Space Technology, 53, 46-60.
Yan, Z. G., Shen, Y., Zhu, H. H., Li, X. J., and Lu, Y., 2015. Experimental investigation of reinforced concrete and hybrid fibre reinforced concrete shield tunnel segments subjected to elevated temperature. Fire Safety Journal, 71(3), 86-99.
Yan, Z. G., Zhu, H. H., and Ju, J. W., 2013. Behavior of reinforced concrete and steel fiber reinforced concrete shield TBM tunnel linings exposed to high temperatures. Construction and Building Materials, 38(2), 610-618.
Yan, Z. G., Zhu, H. H., Ju, J. W., and Ding, W. Q., 2012. Full-scale fire tests of rc metro shield tbm tunnel linings. Construction and Building Materials, 36(4), 484-494.
Yan, Z.G., 2007. A study on mechanical behaviors and fireproof of methods of tunnel lining structure during and after fire scenarios. Doctoral dissertation, Tongji University.
Yin, Y. Z., and Wang, Y. C., 2004. A numerical study of large deflection behaviour of restrained steel beams at elevated temperatures. Journal of Constructional Steel Research, 60(7), 1029-1047.
Yin, Y. Z., and Wang, Y. C., 2005a. Analysis of catenary action in steel beams using a simplified hand calculation method, Part 1: theory and validation for uniform

temperature distribution. Journal of Constructional Steel Research, 61(2), 183-211

Yin, Y. Z., and Wang, Y. C., 2005b. Analysis of catenary action in steel beams using a simplified hand calculation method, part 2: validation for non-uniform temperature distribution. Journal of Constructional Steel Research, 61(2), 213-234.

Zhang, Y., Yan, Z., Ju, J.W., Zhu, H., Chen, Q., 2017. A multi-level micromechanical model for elastic properties of hybrid fiber reinforced concrete. Construction and Building Materials 152, 804–817.

Zhang, Y., Ju, J.W., Zhu, H., Guo, Q., Yan, Z., 2018. Micromechanics based multi-level model for predicting the coefficients of thermal expansion of hybrid fiber reinforced concrete. Construction and Building Materials 190, 948–963.

Zhao, J., Zheng, J. J., and Peng, G. F., 2014. A numerical method for predicting young's modulus of heated cement paste. Construction and Building Materials, 54(54), 197-201.

Zhao, J., Zheng, J. J., Peng, G. F., and Breugel, K. V., 2012. Prediction of thermal decomposition of hardened cement paste. Journal of Materials in Civil Engineering, 24(5), 592-598.

Zhu, H. H., Yan, Z. G., Liao, S. M., Liu, F. J., and Zeng, L. J., 2006. Numerical Analysis and Field Test on Performance of Steel Fibre Reinforced Concrete Segment in Subway Tunnel. Geoshanghai International Conference (pp.248-255).

Zhu, H.H., 1995. Designs and analysis on underground structures. Geo-research institute Report, Osaka, Japan.

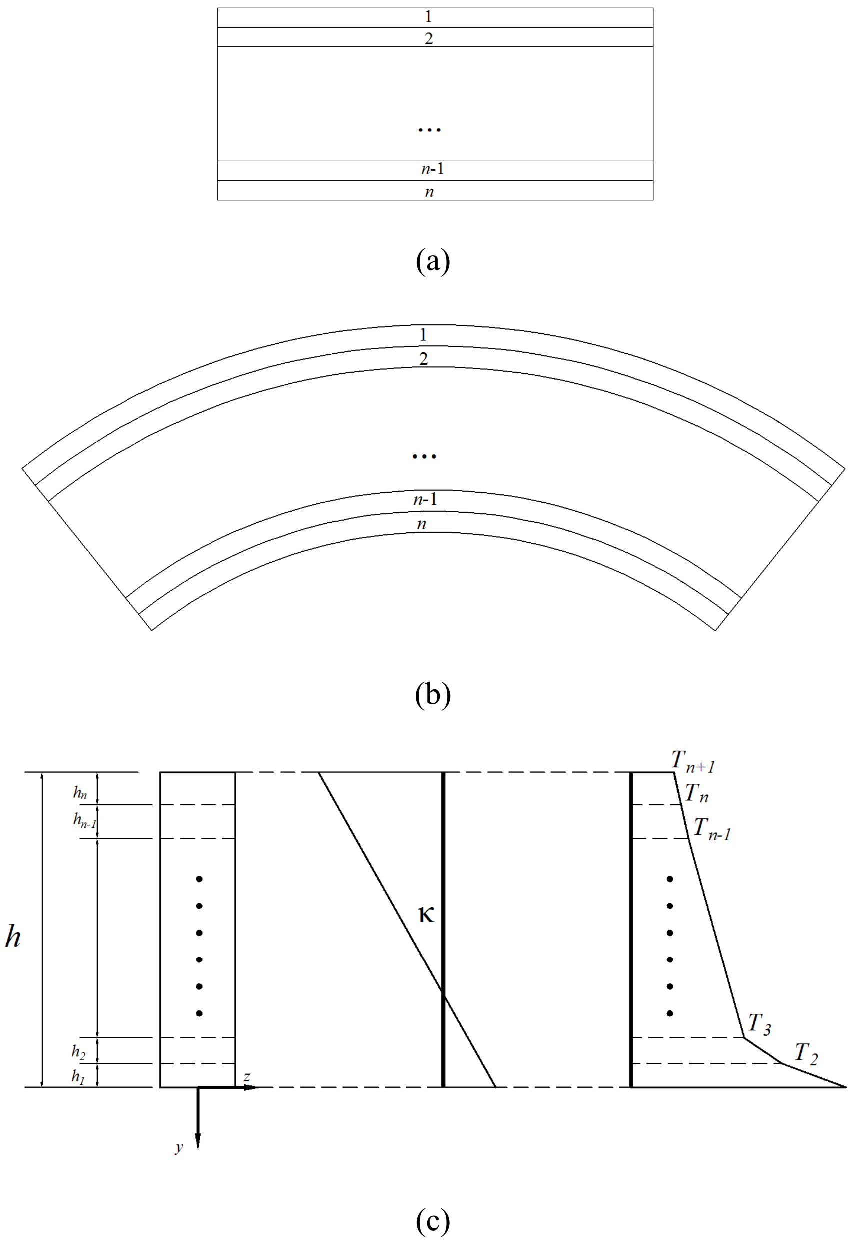


Fig.1. Outline of the model: (a) Layering of the cross section of the tunnel segment; (b) Layering of the profile of the tunnel segment; (c) Strain and temperature distribution over the cross section of tunnel lining segment.

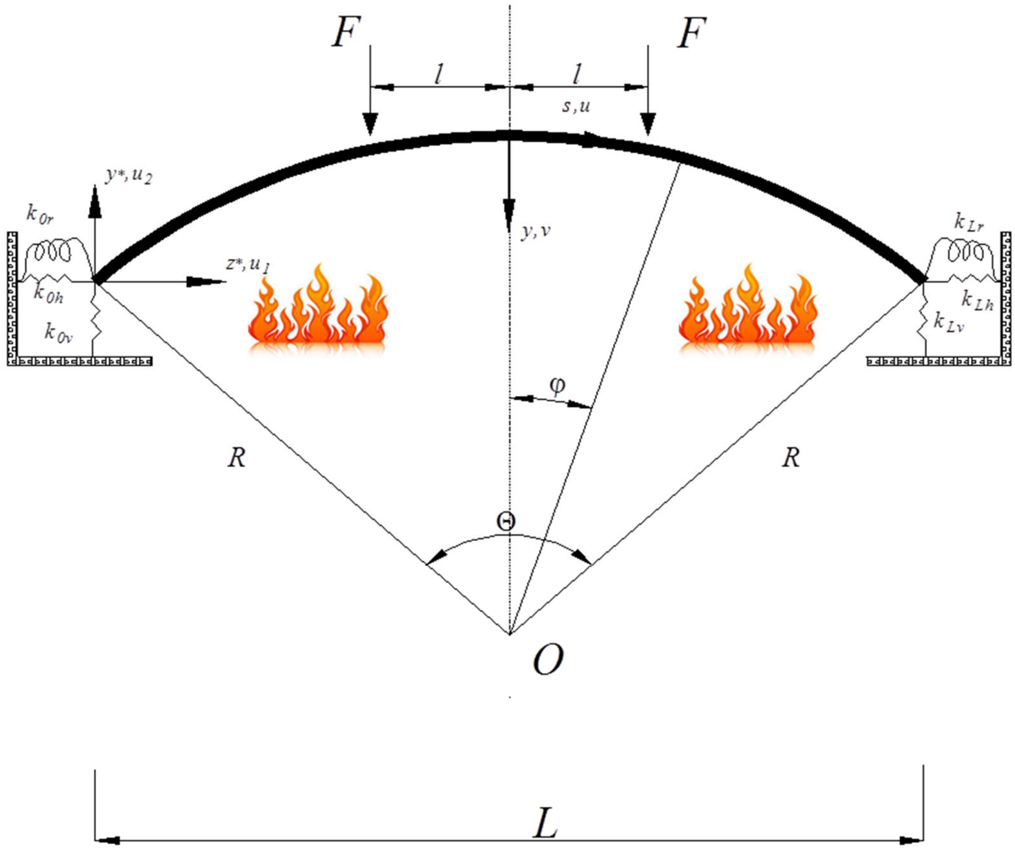


Fig.2. Tunnel lining segment with general boundary conditions.

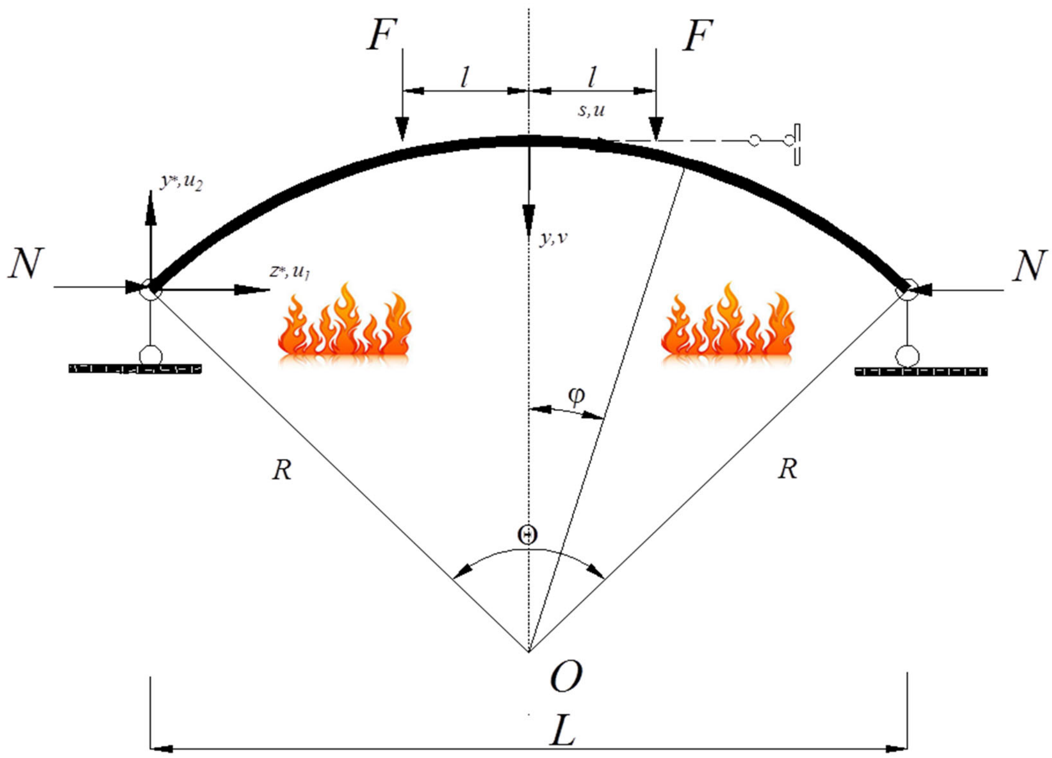


Fig.3. Statically determinate tunnel lining segment.

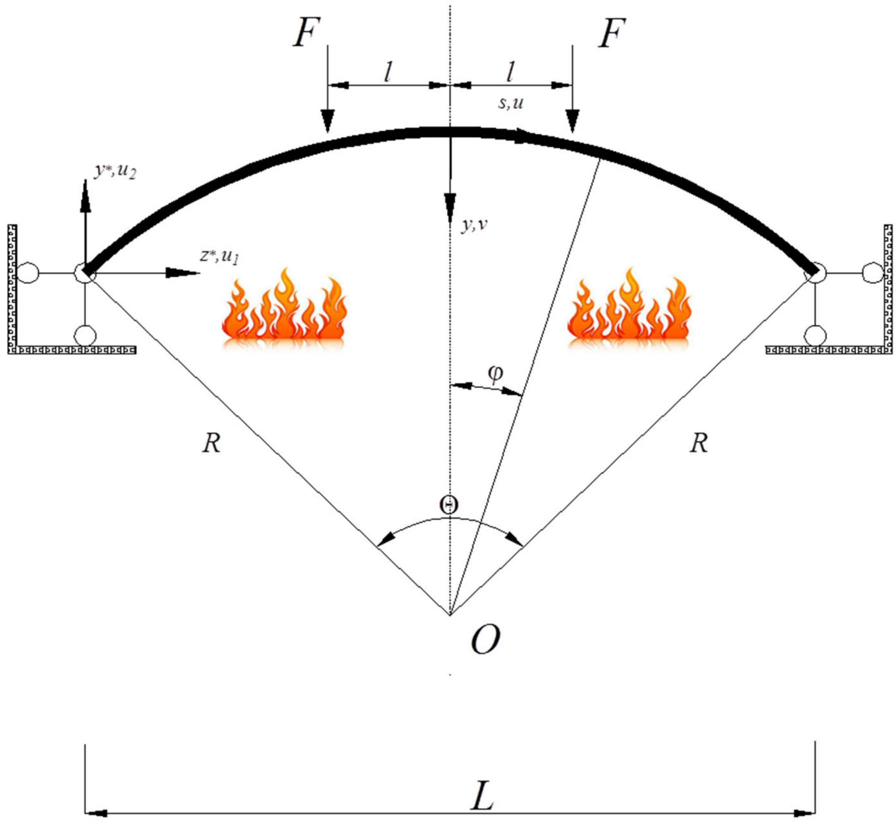

Fig.4. Tunnel lining segment with two hinged ends.

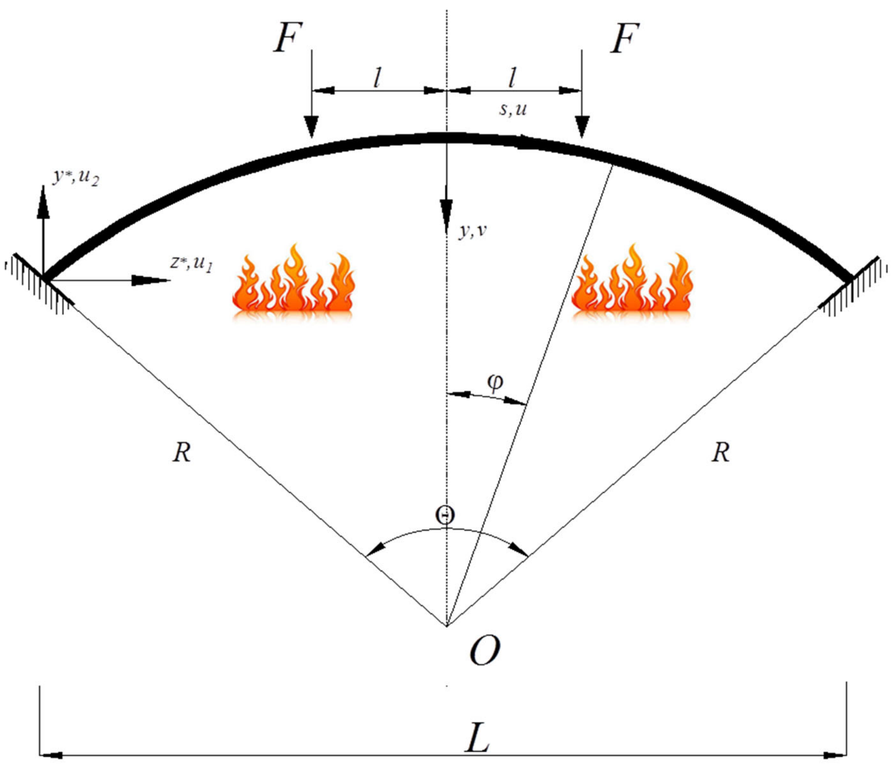


Fig.5. Tunnel lining segment with two fixed ends.

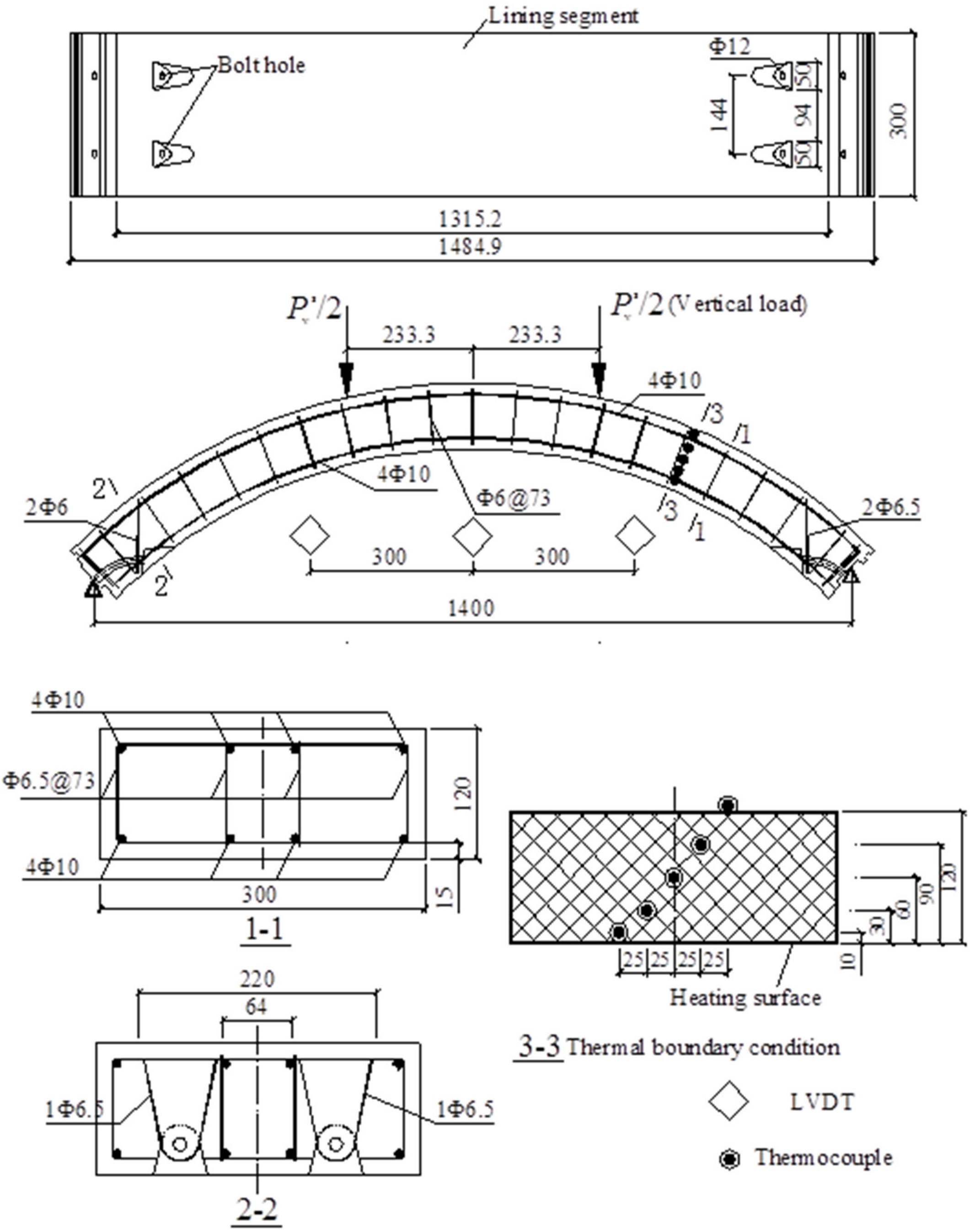


Fig. 6. Geometry and reinforcement details of the concrete lining segment specimens (Dimension: mm).

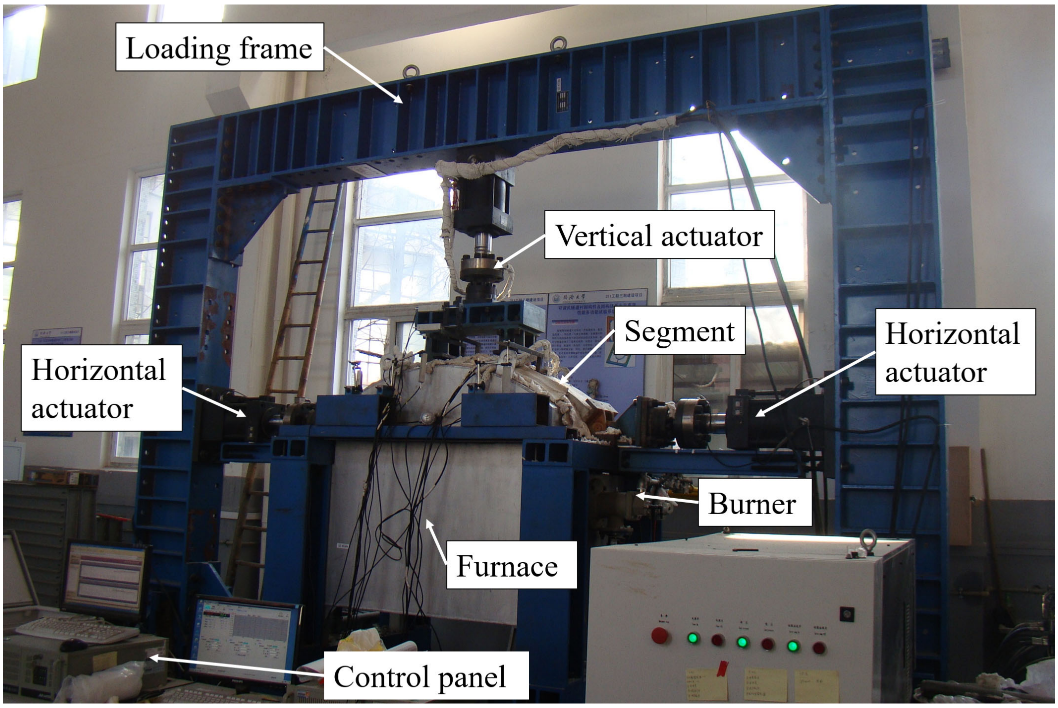


(a)

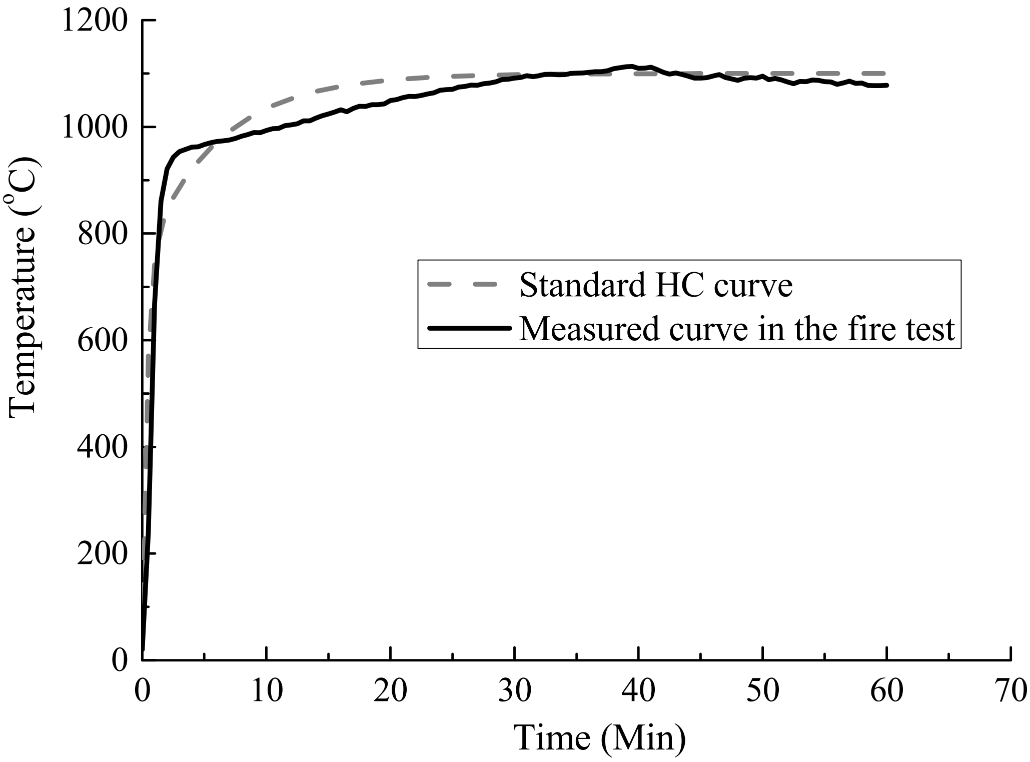


(b)

Fig. 7. Test setup for combined mechanical and thermal loadings and support conditions. (a) Overall view of the test setup. (b) Temperature in the furnace in the test and standard HC curve.

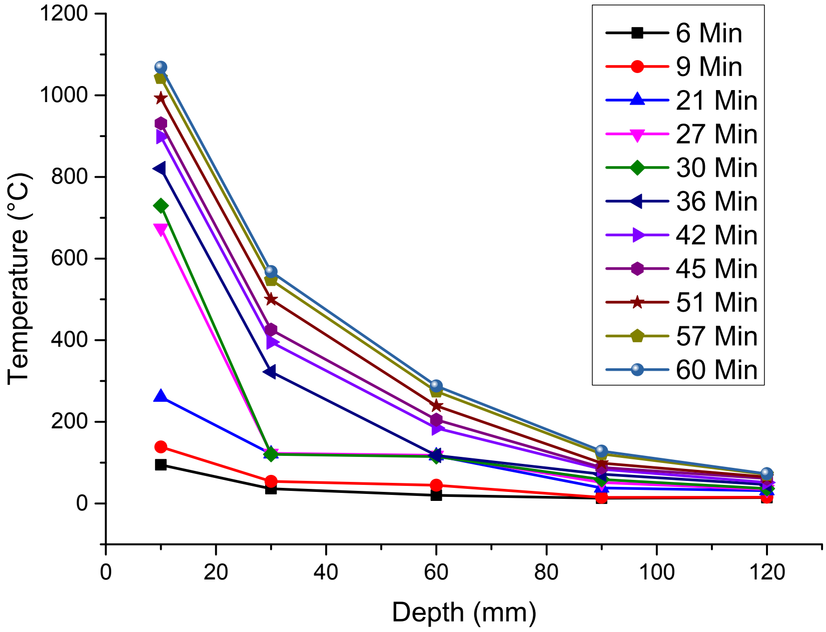


Fig.8 Measured temperature distribution over the cross section.

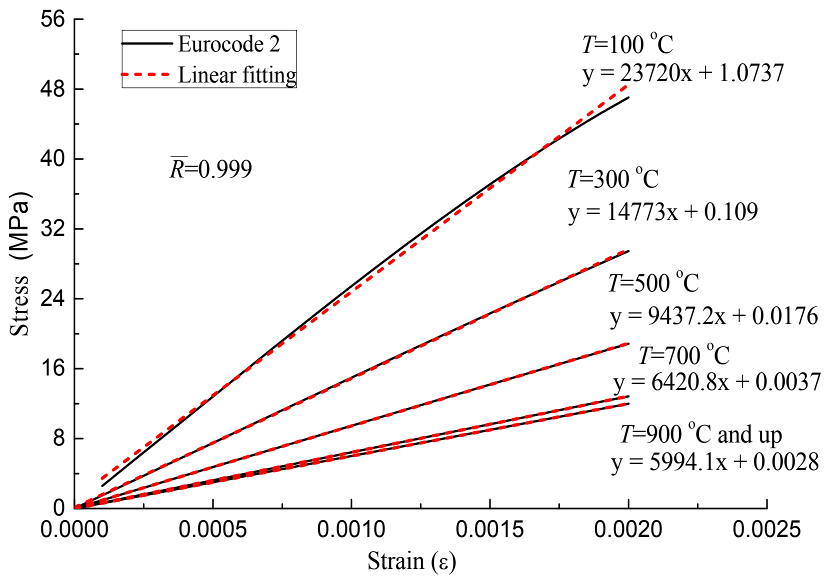


Fig.9. Compressive stress-strain relations of concrete under different temperatures.

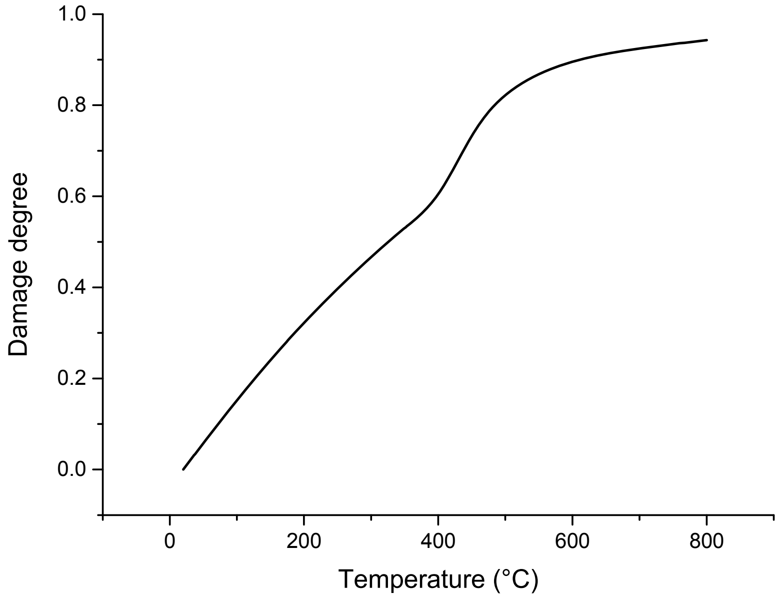


Fig.10 Damage evolution of concrete with temperature.

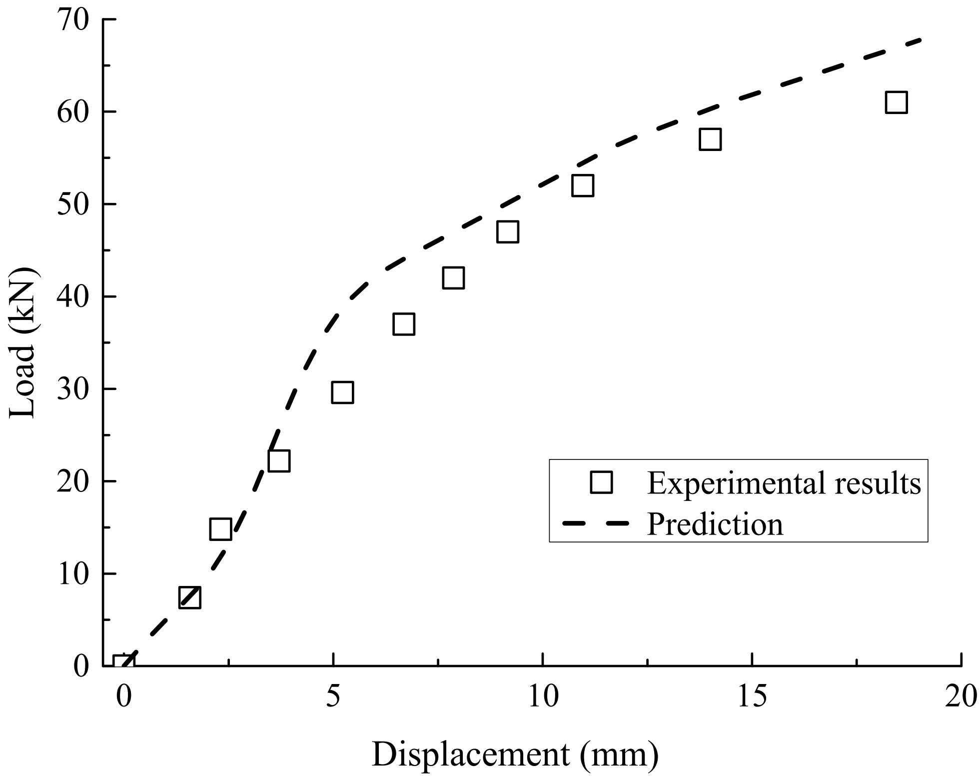


Fig.11. Experimental and predicted displacements at the mid span of RC1.

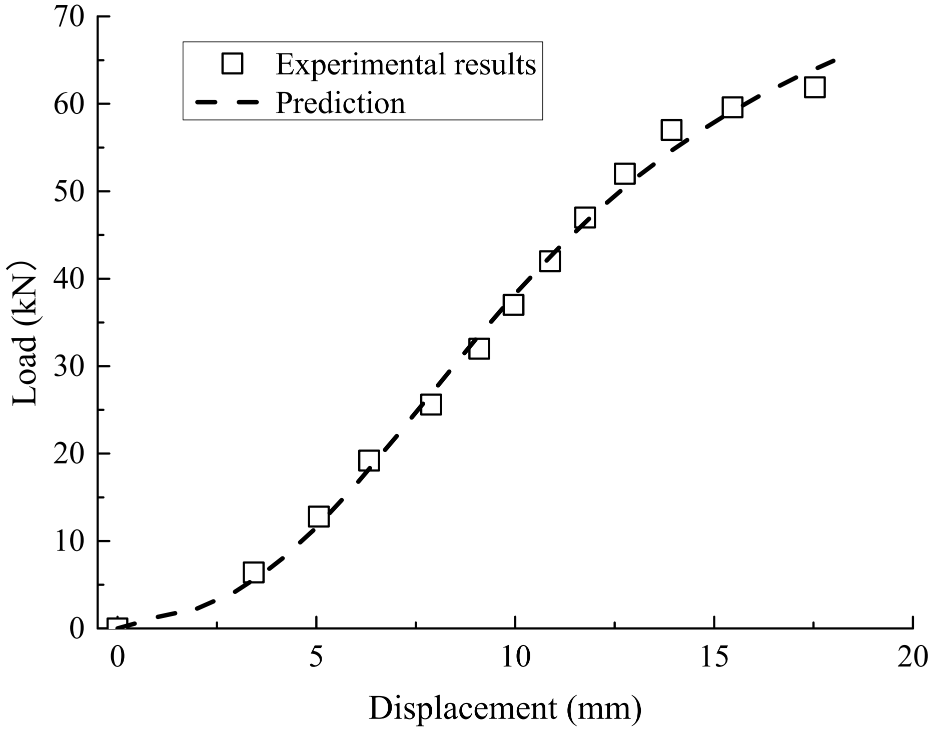

Fig.12. Experimental and predicted displacements at the mid span of RC5.

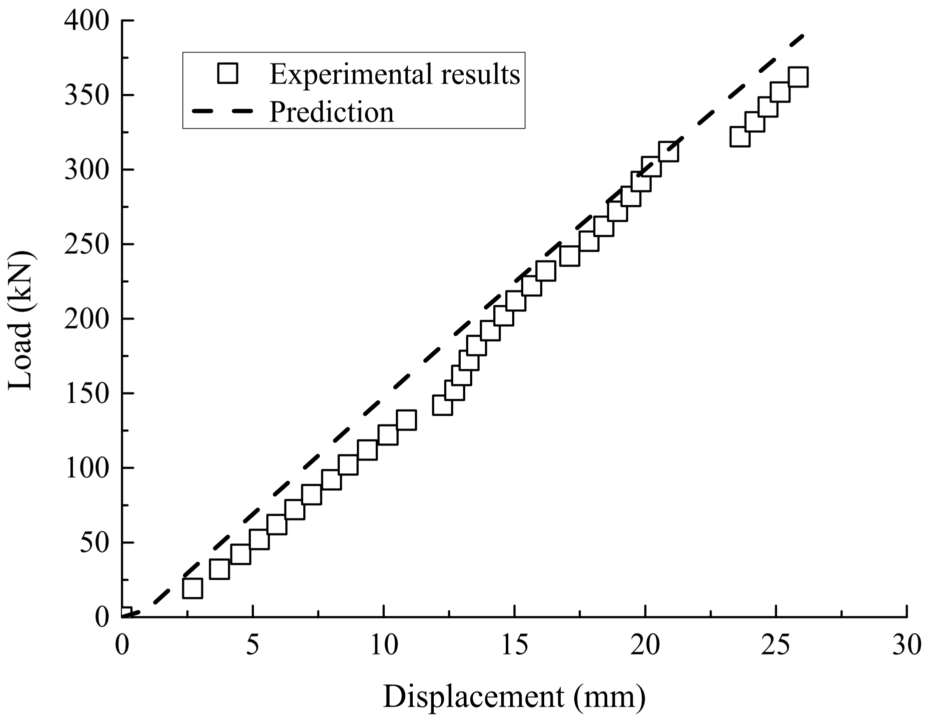

Fig.13. Experimental and predicted displacements at the mid span of RC4.